WAVELENGTH DEPENDENCE OF THE SPECTRAL LINEWIDTH OF A GRATING-TUNED *CW* SINGLE-FREQUENCY EXTERNAL-CAVITY STRAINED QUANTUM WELL *InGaAs/AlGaAs GRINSCH* DIODE LASER

by

LONG HSU

B.S., National Chiao-Tung University, Taiwan, R.O.C.(1980)
M.S., University of New Mexico (1986)

SUBMITTED TO THE DEPARTMENT OF PHYSICS IN PARTIAL FULFILLMENT OF THE REQUIREMENT FOR THE DEGREE OF

DOCTOR OF PHILOSOPHY

at the

MASSACHUSETTS INSTITUTE OF TECHNOLOGY

May 1994

Signature of Author _____
Department of Physics
May 12, 1994

Certified by _____
Roshan L. Aggarwal
Thesis Supervisor

Accepted by _____
Chairman, Departmental Committee on Graduate Students

WAVELENGTH DEPENDENCE OF THE SPECTRAL LINEWIDTH OF A GRATING-TUNED *CW* SINGLE-FREQUENCY EXTERNAL-CAVITY STRAINED QUANTUM WELL *InGaAs/AlGaAs GRINSCH* DIODE LASER

by

LONG HSU

Submitted to the Department of Physics
on May 12, 1994 in partial fulfillment of the requirements
for the degree of Doctor of Philosophy

ABSTRACT

We have measured the wavelength dependence of the spectral linewidth of a grating-tuned *CW* single-frequency external-cavity strained quantum well *InGaAs/AlGaAs* graded-index separate confinement heterostructure (*GRINSCH*) diode laser operating in the wavelength range from *935 to 945 nm* at room temperature, using the heterodyne technique with two free-running lasers. The observed linewidth of the heterodyne beat signal of the two lasers is *Lorentzian* and displays two components: laser power-independent and laser power-dependent. Within the tuning range, this linewidth is found to remain essentially constant at approximately *10 kHz* at laser photon energies well above the energy bandgap and exhibits a sharp rise as the photon energy approaches the band gap. The wavelength dependence of the measured linewidth is consistent with the calculated linewidth. However, the magnitude of the power-dependent component of the measured linewidth exceeds the calculated linewidth due to spontaneous emission by a factor of about 68 ± 9. The power-independent linewidth was interpreted by *Welford and Mooradian* as due to shot noise caused by the statistical fluctuations in the carrier population This concept of shot noise is extended to account for the additional broadening for the power-dependent component of the observed linewidth in this work. Including the shot noise as well as the spontaneous emission, the observed values are then *~10* times lower than the calculated values for the two components of the observed linewidth. This may imply that the shot noise is significantly suppressed.

Thesis Supervisor: Roshan L. Aggarwal
Title: Senior Lecturer

ACKNOWLEDGMENTS

This thesis is a result of my graduate studies at M.I.T. I would like to take this chance to express my deep gratitude to all those who contributed to my work in different perspectives during these years.

I am very honored to be advised by some of M.I.T. teachers whom are out of question among the greatest physicists in the world. I hope that I can emulate them in the future.

First of all, I thank Dr. James Small, who was my Master Degree thesis advisor at the University of New Mexico and who is also a M.I.T. alumni. Without his teaching, guidance, and strong recommendation, I would not be here at M.I.T.

Prof. Dan Kleppner was my advisor for my first three years at M.I.T. as well as one of my current thesis committee member. He has been very patient, understanding, and helpful to me. He gave me a hand at my worst time and helped my out. I am grateful to what he has done for me and I will try to be as a great teacher as he has been to me when given the opportunity. Furthermore, Prof. Kleppner and my other thesis committee member, Prof. Ogilvie gave me very valuable opinions on this manuscript. I thank them for their helpful suggestions.

Prof. Aram Mooradian lead me into group 82 of Lincoln Laboratory. He initiate this study as well as the experiment. He taught me so much and I deeply appreciated his guidance at the beginning stage.

Dr. Roshan Aggarwal, my thesis advisor, has been extremely supportive and helpful to my work. Whenever I had a problem, he was always there and willing to give me guidance and support even when his health condition was at risk. He gave me much valuable advice for my study and was very patient when the progress was slow. He was always very eager to find out the answers to the questions raised.. He is one of the greatest teacher as well as physicist I have ever work with and I give him my salute and best wish to his health. Without his supervision, this study could not have been possible.

His careful and patient proof-reading of this manuscript greatly improved its quality. I am deeply indebted to him.

I also benefited greatly from the intellectual and friendly community of group 82 of Lincoln Laboratory under the leadership of Dr. Antonio Sanchez-Rubio. Antonio gave me continuous support for which I greatly appreciated. Dr. Tso Yee Fan was very helpful during the whole study. He has a very broad knowledge of Quantum Electronics and offered me very valuable advice. He was also very patient listening to my presentation while helping to improve my presentation skills. I am grateful to his help. I also gained a lot of information from discussion with Dr. J. Zayhowski, Dr. D. Nabors, Dr. V. Daneu, Dr. H. Lee, and Dr. T. Jeys. Christ Cook made extremely good coating on the diodes for me, which quickened the progress of the study. I thank him for his contribution. I also appreciate all other group members' support, encouragement, and friendship. They made my life at M.I.T. much easier and tolerable. Colby Dill and Juan Ochoa, my comrades at arms, were always there when I needed any help. Sal DiCecca offers me rides and teaches me Italian. John Daneu and Bill DeFeo introduce to me many interesting things about plants and nature. Jane Galus is very kind and always willing to help. It was a great joy working in this group with all those friends. I thank them all.

My three children, Yu, Ming, and Chang, are wonderful presents to me. It was such a joy when I heard their sweet voice saying prayer together and "Good-Night, Daddy!" over the phone. I will certainly miss that. My wife, Jane, takes care of everything for me, so that I can concentrate in study only. I don't know how to express my thank and appreciation to her.

My parents firmly supported my studies and research at M.I.T. as they always have supported me in the past. It has been a long road and I can never thank them enough even by dedicating this thesis to them.

Finally, and most importantly, I acknowledge that there was God's work in here. After I received my Ph.D., I wish I could contribute more to others than to myself.

May 1994 Long Hsu

TABLE OF CONTENTS

		Page
Title Page		1
Abstract		3
Acknowledgments		5
Table of Contents		9
List of Figures		11
List of Tables		15
Chapter 1:	Introduction	17
Chapter 2:	Theory of the Laser Linewidth	21
2.1	Power-Dependent Linewidth due to Phase Noise	21
2.2	Power-Dependent Linewidth due to Amplitude Noise	32
2.3	Power-Dependent Linewidth due to Shot Noise	37
Chapter 3:	Simple Interband Model for the Calculation of Amplitude-Phase Coupling Factor α	40
3.1	Band Structure of Semiconductor	40
3.2	Physical Structure of a Quantum-Well Diode Laser with Graded-Index Separate Confinement Heterostructure (*GRINSCH*)	44
3.3	Effects of Alloy Composition and Strain due to Lattice Mismatch	49
3.4	Input, Intermediate, and Output Parameters	53
3.5	Calculated Amplitude-Phase Coupling Factor α and Linewidth Versus Wavelength	58
Chapter 4:	Experimental Procedure	61
4.1	Design of Grating-Tuned External-Cavity Diode Laser	61
4.2	Measurement of the Threshold Current	67
4.3	Measurement of the Laser Linewidth using Heterodyne Technique with Two Free-Running Lasers	69
Chapter 5:	Results and Discussion	75
Chapter 6:	Conclusions	89
References		91

LIST OF FIGURES

Number	Caption	Page
2.1	Complex representation of the electric field β. The i^{th} spontaneous emission event results in instantaneous changes in the electric field amplitude $\sqrt{I_\beta} \rightarrow \sqrt{I_\beta + \Delta I_{\beta_i}}$ and phase $\varphi \rightarrow (\varphi + \Delta\varphi_i)$.	24
2.2	A schematic of a laser with a composite cavity.	30
2.3	Dispersion of real part χ_l' and imaginary part χ_l'' of the electric susceptibility for (a) a semiconductor laser, and (b) a gas or solid-state laser.	36
3.1	(a) A typical energy band structure for a bulk III-V semiconductor, and (b) Quasi-*Fermi* energies and *Fermi-Dirac* occupation factors for electrons and holes.	41
3.2	(a) Alloy composition structure along the crystal growth direction, and (b) a typical quantum-well diode laser with *GRINSCH* structure.	45
3.3	(a) The conduction and valence band edges under forward bias in a quantum-well *GRINSCH* $In_xGa_{1-x}As/Al_yGa_{1-y}As$ laser diode, and (b) the static refractive index profile and the optical field (fundamental mode) profile. Waveguiding effect contributes to the optical energy confinement in the active layer as shaded.	46
3.4	(a) Quantization of the energy levels for electrons, *HH* and *LH* in a quantum well, and (b) schematic representation of the parabolic subbands.	47
3.5	(a) Compressive strain and lattice deformation. Tetragonal distortion due to the application of two-dimensional stress to a cubic crystal. Note that the epitaxial layer contracts in the interfacial plane but expands in the vertical plane, and (b) biaxial strain-induced shift and splitting S of the valence bands.	49
3.6	Calculated (a) $\Delta\chi_l'\|_{\Delta N}$, (b) $\Delta\chi_l''\|_{\Delta N}$, and (c) α as a function of wavelength at threshold condition, using $x = 0.14$ and $T_2 = 1 \times 10^{-13}$ *sec*, and $\Delta N = 1 \times 10^{15}\ cm^{-3}$.	59
3.7	Calculated linewidth due to spontaneous emission versus wavelength for $x = 0.14$ and $x = 0.16$.	60

Number	Caption	Page
4.1	Schematic of the grating-tuned external-cavity diode laser.	63
4.2	(a) Section of a blazed grating, and (b) the *Littrow* autocollimation mounting.	65
4.3	Acoustic isolation arrangement.	66
4.4	Block diagram of the setup for threshold current measurement.	67
4.5	Plot of laser output power as a function of injection current.	68
4.6	Block diagram of the heterodyne setup.	74
5.1	Plot of laser output power as a function of wavelength for laser diode #1.	76
5.2	Comparison between the measured (dots) and the calculated (solid curves) threshold current I_{th} as a function of wavelength λ, using $x = 0.16$ for laser #1.	77
5.3	Heterodyne beat signal between two free-running external-cavity diode lasers *#1* and *#2* at *940 nm* for different output powers. The thick black solid curves are *Lorentzian* fits to the data: (a) through (d).	78
5.4	Frequency jitter between two free-running *InGaAs* external-cavity diode lasers.	80
5.5	Measured linewidth of the heterodyne beat signal as a function of inverse output power.	81
5.6	Measured (dots) and calculated [solid curve: $\Delta\nu_1(x=0.14) + \Delta\nu_2(x=0.16)$ with $f = 77$ and $\Delta\nu_{PJ} = 6$ *kHz*] linewidth (*FWHM*) of the heterodyne beat signal as a function of wavelength.	83

LIST OF TABLES

Number	Contents	Page
3.1	Effective masses in $In_{0.14}Ga_{0.86}As$ for bulk and strained quantum-well configurations.	50
3.2	Material parameters for strained $In_xGa_{1-x}As/GaAs$	52
3.3	Input parameters of the model for the calculation of α.	53
3.4	Intermediate Parameters of the model for the calculation of α	55
3.5	Output parameters of the model for the calculation of α.	57

CHAPTER 1

INTRODUCTION

The spectral linewidth of a laser arises directly from phase noise and indirectly from amplitude noise through amplitude-phase coupling. In addition, the fluctuations in the cavity frequency arising from the fluctuations in the refractive index of the laser medium and/or the cavity length also result in the spectral linewidth broadening. The sources of noise are classified into two categories: extrinsic and intrinsic. The extrinsic noise sources include the current source noise, temperature noise, and acoustic (vibrational) noise. In this work, the laser diode was driven with an ultra-stable current source and thermally controlled by a temperature regulator. The laser was operated on an aluminum plate atop a box of sand and within a plexiglass enclosure, which was mounted on a laser table. Therefore, the extrinsic noise is assumed to be negligible in comparison with the intrinsic noise.

The intrinsic noise sources include the instantaneous phase noise and amplitude (intensity) noise due to spontaneous emission, which result in a *Lorentzian* power-dependent linewidth. However, the model[1-3] based on spontaneous emission fails in interpreting the additional broadening for the power-dependent component of the observed linewidth in this work and the unexpected power-independent component of the linewidth observed previously and in this work. The power-independent linewidth was interpreted by *Welford and Mooradian*[4] as due to shot noise caused by the statistical fluctuations in the carrier population. This concept of shot noise as an additional intrinsic noise source is extended to account for the additional contribution to the power-dependent linewidth observed in this work.

The transformation of phase noise to optical linewidth results in the well-known power-dependent *Shawlow-Townes*[1] linewidth $\Delta\nu_{S\text{-}T}$, in which only the instantaneous phase noise due to spontaneous emission is considered. The instantaneous amplitude noise due to spontaneous emission induces a delayed phase noise (*AM-FM* coupling) through the fluctuations in population inversion $\Delta\eta_{sp}$, which is characterized by *Henry*'s[2] α. This delayed phase noise causes additional linewidth $\alpha^2\Delta\nu_{S\text{-}T}$ through the same *Shawlow-Townes*'s phase-linewidth transformation. The shot noise due to statistical fluctuations in the carrier population $\Delta\eta_{stat}$ is converted to the intensity (amplitude) noise. This intensity noise, in turn, follows the *AM-FM* coupling and thus brings in the third component $f\alpha^2\Delta\nu_{S\text{-}T}$ to the linewidth; here f is the ratio of $\Delta\eta_{stat}$ to $\Delta\eta_{sp}$. Because the three sources of phase noise go through the same final channel $(\Delta\nu_{S-T})$ leading to the linewidth, their corresponding linewidths are referred to as the power-dependent linewidths. Consequently, the overall intrinsic linewidth is the sum of the power-dependent linewidth and the power-independent linewidth.

The resulting linewidth broadening due to α and f is quite significant and wavelength-dependent for the semiconductor diode laser; the variation of $\Delta\nu_{S\text{-}T}$ within a few percent tuning range of a laser is negligible. On the contrary, $\alpha = 0$ at the resonant frequency for gas and solid-state lasers which are operated at the frequency where the maximum gain is. For many applications, wavelength tunability is an important requirement of the semiconductor laser. A semiconductor diode laser in an external cavity not only allows wavelength tuning but also results in considerable line narrowing. Therefore, it is important to study the wavelength dependence of the linewidth of a tunable diode laser in an external cavity.

In this work we have studied the wavelength dependence of spectral linewidth of a grating-tuned *CW* single-frequency external-cavity strained quantum-well

$In_xGa_{1-x}As$ / $Al_yGa_{1-y}As$ graded-index separate confinement heterostructure (*GRINSCH*) diode laser operating in the wavelength range from *935* to *945 nm* at room temperature. The minimum threshold current has been found to be as low as *40 mA* and the minimum linewidth of the heterodyne beat signal has been found to be as narrow as *~10 kHz* at *5 mW* for laser wavelengths below *940 nm*.

The work involves: a) design and construction of two grating-tuned free-running external-cavity diode lasers, b) measurements of threshold current and spectral linewidth using heterodyne technique with two lasers, c) calculation of the threshold current, the amplitude-phase coupling factor α, and the linewidth, and d) comparison of the calculated values with the measured values as a function of wavelength.

The linewidth of the heterodyne beat signal of the two lasers is found to remain essentially constant at approximately *10 kHz* at laser photon energies well above the energy bandgap of the semiconductor and exhibits a sharp rise as the photon energy approaches the band gap. The wavelength dependence of the measured linewidth is consistent with the calculated linewidth. However, the magnitude of the measured power-dependent linewidth exceeds the calculated linewidth due to spontaneous emission by a factor of about 68 ± 9. After including the shot noise contribution, this measured value turns out to be approximately *10* times smaller. This may imply that *90%* of the shot noise is suppressed.

The remainder of this thesis is divided into five Chapters. Chapter 2 provides a theoretical background on the *Shawlow-Townes* linewidth $\Delta\nu_{S\text{-}T}$, which serves as the last channel leading to the power-dependent linewidth. The relationship between α and the energy band structure of the laser medium is discussed. This explains the vanishing of linewidth enhancement at peak gain in gas and solid-state lasers. The physics behind the

proposed shot noise model is explained and the analytical expression for its corresponding linewidth is derived accordingly. Chapter 3 describes the model for the calculation of α in this work. The model includes the effects of alloy composition, strain due to lattice-mismatch, and *GRINSCH* quantum-well structure. Wavelength dependence of α and the threshold current are calculated.

Chapter 4 describes the experimental apparatus and procedure. The design of the grating-tuned external-cavity diode laser for a stable *CW* single-frequency operation is described. A series of experiments have been conducted with two free-running grating-tuned external-cavity diode lasers. Chapter 5 presents the experimental results and the comparison between the data and the calculations based on the proposed model. Finally, in Chapter 6, concluding comments offer a brief review of the most important results. Some comments for future work are also given.

CHAPTER 2

THEORY OF THE LASER LINEWIDTH

One of the most important properties of laser light is its spectral purity, which is characterized by its spectral linewidth. This property is important for laser applications such as high-resolution spectroscopy and interferometry.

2.1 Power-Dependent Linewidth due to Phase Noise

Interest in the linewidth was present prior to the invention of laser physics. *Schawlow* and *Townes*[1] first predicted the *Lorentzian* power spectrum of the laser field and the inverse dependence of the spectral linewidth on laser power. *Lax*[2] pointed out that this formula is only valid for operation below threshold. *Lax*'s formalism for operation above threshold is referred to as the modified *Schawlow-Townes* linewidth $\Delta\nu_{S-T}$. In this section, a common model is presented for the modified *Schawlow-Townes* linewidth, which is adequate for all types of lasers and serves as the last channel connecting the phase noise to the spectral linewidth for the following amplitude (intensity) noise and shot noise.

To understand how the spontaneous emission broadens the laser linewidth, consider the phase evolution of the electric field $E(r, t)$ of the laser radiation. In the absence of phase noise, the phase of the field evolves with time at a constant frequency ν. However, in the presence of spontaneous emission, which continuously alters the phase and amplitude of the field, the uniform evolution of the phase is interrupted. The

variation of phase in time domain can be *Fourier* transformed into frequency domain, which results in a finite spectral width $\Delta\nu$.

Quantitatively, the derivation of laser linewidth begins with the field $E(r, t)$ in a laser medium, which is given in a generalized form

$$E(r, t) = A(r)\, e^{i[\omega_l t - kr + \varphi(r, t)]} + a(r, t)\, e^{i[\omega_l t - kr + \varphi(r, t)]}, \tag{2.1}$$

with

$$\omega_l = 2\pi\nu_l = \frac{2\pi c}{\lambda_l}, \tag{2.2}$$

where A, ω_l, and k are the amplitude, angular frequency, and complex wave vector of the laser field in the medium respectively, a and φ are the amplitude and phase noises respectively, c is the speed of light in vacuum, ν_l and λ_l are the frequency and vacuum wavelength of the laser field respectively, and the subscript l denotes the presence of laser action. Assume that $a(r, t) << A(r)$ and $\dot{\varphi}(r, t) << \omega_l$, where $\dot{\varphi}$ is the time derivative of φ.

Both the phase noise and the amplitude noise contribute to the spectral linewidth. However, the latter occurs through an amplitude-phase (*AM-FM*) coupling, which is less obvious. This is why *Schawlow* and *Townes* considered only the first component in Eq. (2.1), which represents the instantaneous phase noise due to spontaneous emission. The second component involving the amplitude noise a is treated in *Henry*'s amplitude-phase coupling factor α in the next section.

Following the notation of *Henry*,[3] the electric field E is normalized so that the energy intensity I_β of the normalized field β is equal to the number of photons N_{ph} in the laser cavity:

$$I_\beta = \frac{1}{2}\varepsilon_l \beta^* \beta \equiv N_{ph}, \tag{2.3}$$

where ε_l is the dielectric constant of the medium in the presence of laser. The normalized field β is chosen to retain the phase noise φ(t) of E such that

$$\beta(t) = \sqrt{I_\beta}\, e^{i\varphi(t)}. \tag{2.4}$$

Combining Eq.(2.1) for E with Eq. (2.3) for β, the relationship between the two fields is given by

$$E(t) = \frac{[A + a(t)]}{\sqrt{I_\beta}}\, e^{i\omega_l t}\beta(t). \tag{2.5}$$

The variable r in Eq. (2.5) is dropped because of irrelevance.

The result of a single spontaneous emission event is illustrated in Fig. 2.1. The field perturbation due to the i^{th} spontaneous emission event alters β by $\Delta\beta_i$. The advantage of the normalization of E to β is that $\Delta\beta_i$ has a unit magnitude and a random phase:

$$|\Delta\beta_i| = 1 \tag{2.6}$$

$$\Delta\beta_i = 1 \cdot e^{(i\varphi + i\theta_i)}, \tag{2.7}$$

where θ_i is random. This corresponds to instantaneous changes in the intensity ΔI_{β_i} and phase $\Delta\phi_i$:

$$\Delta I_{\beta_i} = 2\sqrt{I_\beta}\, \cos\theta_i + 1, \tag{2.8}$$

$$\Delta\varphi_i = \frac{\sin\theta_i}{\sqrt{I_\beta}}. \tag{2.9}$$

These changes occur at random times t_i; the average rate of spontaneous emission events is taken to be R_{sp}.

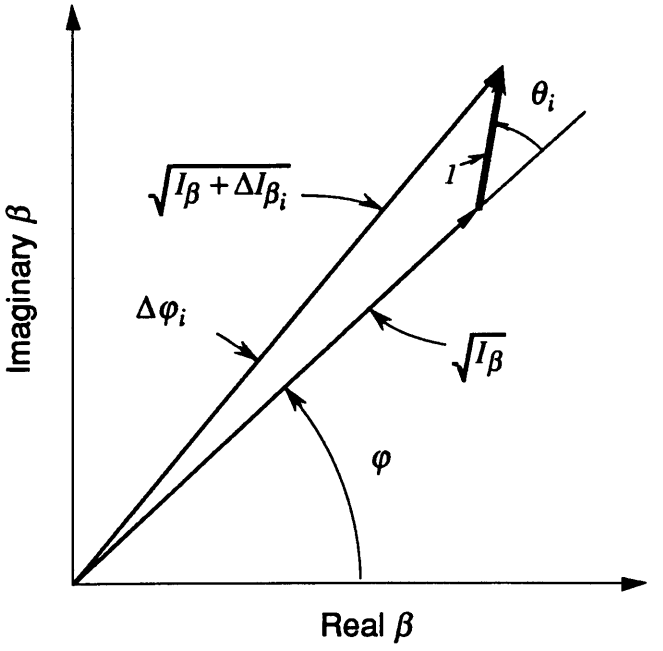

Fig. 2.1 Complex representation of the field β. The i^{th} spontaneous emission event results in instantaneous changes in the field amplitude $\sqrt{I_\beta} \rightarrow \sqrt{I_\beta + \Delta I_{\beta_i}}$ and phase $\varphi \rightarrow (\varphi + \Delta\varphi_i)$.

The intensity fluctuations are subject to a strong restoring force because of gain clamping above threshold. That is, the system has a single stable operating point at which gain and loss are balanced. When the field is perturbed by spontaneous emission , the laser undergoes damped relaxation oscillations. This returns the intensity I_β to its steady state but leaves the phase free to drift.

According to the *Wiener-Khintchine* theorem,[5] the power spectrum of the field $S_p(\nu)$ is given by the *Fourier* transform of the field autocorrelation function$R(\tau)$:

$$S_p(\nu) \equiv \mathcal{F}\{R(\tau)\}, \tag{2.10}$$

with

$$R(\tau) \equiv \lim_{T\to\infty} \frac{1}{2T} \int_{-T}^{T} E(t)E^*(t-\tau)\,dt, \tag{2.11}$$

where $\mathcal{F}\{\ \}$ denotes the *Fourier* transform. Neglecting the amplitude fluctuations ($a << A$), E in Eq. (2.5) becomes

$$E(t) \cong \frac{A}{\sqrt{I_\beta}}\, e^{i\omega_l t}\beta(t). \tag{2.12}$$

Upon substituting for E from Eq. (2.12), Eq. (2.11) for the autocorrelation of $E(t)$ is given by

$$R(\tau) \equiv \lim_{T\to\infty} \frac{1}{2T} \int_{-T}^{T} \left[\frac{A}{\sqrt{I_\beta}}\, e^{i\omega_l t}\beta(t)\right]\left[\frac{A^*}{\sqrt{I_\beta}}\, e^{-i\omega_l(t-\tau)}\beta^*(t-\tau)\right] dt. \tag{2.13}$$

It can be shown that the above equation can be written in the form

$$R(\tau) = |A|^2\, e^{i2\pi\nu_l\tau}\left\langle e^{i\Delta\varphi(\tau)}\right\rangle, \tag{2.14}$$

where the $\langle\ \rangle$ brackets indicate the time averaged value and $\Delta\varphi$ is the phase change within an interval τ defined as

$$\Delta\varphi(\tau) \equiv \varphi(t) - \varphi(t-\tau). \tag{2.15}$$

The solution of Eq. (2.14) requires knowledge of the statistics of the fluctuating variable $\varphi(t)$. Due to the random spontaneous emission events, the phase φ executes *Brownian* motion and has a *Gaussian* probability distribution.[6] The probability distribution function of the phase $f(\varphi(t))$ must satisfy the relation [5]

$$\frac{\partial f(\varphi(t))}{\partial t} = D\frac{\partial^2 f(\varphi(t))}{\partial \varphi^2}, \tag{2.16}$$

where the constant D is referred to as the phase diffusion coefficient and is given by

$$D = \frac{\langle \Delta\varphi^2(\tau) \rangle}{2|\tau|}. \tag{2.17}$$

The solution of Eq. (2.16) is the conditional probability $f(\varphi(t))$ that gives the probability that the phase will be $\varphi(t+\tau)$ at time $(t+\tau)$ given that it was $\varphi(t)$ at an earlier time t. This is given by[6]

$$f(\Delta\varphi(\tau)) = \frac{e^{-[\Delta\varphi^2(\tau)/4D|\tau|]}}{\sqrt{4\pi D|\tau|}}, \tag{2.18}$$

and can be interpreted as a statement that the phase change in time τ is a *Gaussian* process. With $f(\varphi(t))$ of Eq. (2.18), and with the additional assumption that $\Delta\varphi(\tau)$ is a stationary variable, Eq. (2.14) for $R(\tau)$ turns out to be

$$R(\tau) = |A|^2 \, e^{i2\pi\nu_l\tau} \, e^{-D|\tau|}. \tag{2.19}$$

The final step is to complete the *Fourier* transform of $R(\tau)$. Using Eq. (2.19) for $R(\tau)$, the power spectrum of the field $S_p(\nu)$ in Eq. (2.10) can be shown

$$S_p(\nu) = \frac{2|A|^2}{D} \, \frac{1}{1+\left[\frac{(\nu-\nu_l)}{D/2\pi}\right]^2}. \tag{2.20}$$

The lineshape of $S_p(\nu)$ is *Lorentzian* centered at ν_l with linewidth (full width at half of the maximum intensity *FWHM*) is given by

$$\Delta\nu_{FWHM} = \frac{D}{\pi} = \frac{\left\langle \Delta\varphi^2(\tau) \right\rangle}{2\pi|\tau|}. \tag{2.21}$$

To express the linewidth in terms of measurable laser parameters, it is necessary to evaluate $\left\langle \Delta\varphi^2(\tau) \right\rangle$ according to Eq. (2.9) for $\Delta\varphi$. Because θ_i associated with each event is random as shown in Fig. 2.1, the time average of $\Delta\varphi^2$ is performed in the limiting case of infinite events

$$\left\langle \Delta\varphi^2(\tau) \right\rangle = \lim_{R_{sp}|\tau|\to\infty} \left[\sum_{i=1}^{R_{sp}|\tau|} \sum_{j=1}^{R_{sp}|\tau|} \frac{\sin\theta_i}{\sqrt{I}} \frac{\sin\theta_j}{\sqrt{I}} \right] = \frac{R_{sp}|\tau|}{2I}, \tag{2.22}$$

where I is the number of photons in the cavity and the subscript β is dropped from now on for simplicity. Substituting Eq. (2.22) into Eq. (2.21), the modified *Shawlow-Townes* linewidth has simple form

$$\Delta\nu_{S-T}(FWHM) = \frac{R_{sp}}{4\pi I}. \tag{2.23}$$

Referring to *Yariv*[7], the rate of the spontaneous emission R_{sp} per mode is related to the net rate of the stimulated emission per photon in the same mode G as given by

$$R_{sp} = n_{sp}\, G, \tag{2.24}$$

with

$$n_{sp} = \frac{N_u}{N_u - N_l}, \tag{2.25}$$

where N_u and N_l are the occupation densities of the upper and lower states of the laser transition, respectively. The proportionality constant n_{sp} between R_{sp} and G is referred to as the spontaneous emission factor,[3,8] which reflects the degree of population inversion.

For a strained quantum-well *InGaAs/AlGaAs* laser[9,10] used in this experiment, $n_{sp} \cong 1$ and does not play an important role in the wavelength dependence of laser linewidth.

The net rate of stimulated emission G per photon is given by

$$G = v_g \times g_{th}, \tag{2.26}$$

with

$$v_g = \frac{c}{n_l'}, \tag{2.27}$$

and

$$g_{th} = \gamma + \frac{1}{2L}\ln\left(\frac{1}{R_1 R_2}\right), \tag{2.28}$$

where v_g is the group velocity of light in the active medium, n_l' is the real part of the refractive index of the active medium, g_{th} and γ are the threshold gain and the internal loss coefficient of the medium, respectively, L is the cavity length of the medium, and R_1 and R_2 are the reflectances of the two end mirrors of the laser cavity respectively. Here the subscript l in n_l' denotes the presence of laser action. It should be pointed out that n_l' as shown above is the phase refractive index for simplicity.

For a homogeneous laser medium, it can be shown that the number of photon I in the cavity is related to the total output power P_o by

$$I = \frac{P_o}{h\nu_l \gamma_m}\left(\frac{n_l'}{c}\right) \tag{2.29}$$

with

$$\gamma_m \equiv \frac{1}{2L}\ln\left(\frac{1}{R_1 R_2}\right), \tag{2.30}$$

where h is the *Plank*'s constant and γ_m is the distributed mirror loss coefficient.

Substituting Eq. (2.24) for R and Eq. (2.29) for I, the *Shawlow-Townes* linewidth in Eq. (2.23) is given by

$$\Delta\nu_{S-T}(\lambda_l) = \frac{hc}{8\pi P_o \lambda_l}\left(\frac{c}{n_l' L}\right)^2\left[\gamma L + \frac{1}{2}\ln\left(\frac{1}{R_1 R_2}\right)\right]\ln\left(\frac{1}{R_1 R_2}\right) n_{sp}. \tag{2.31}$$

The laser linewidth $\Delta\nu_{S-T}$ as shown above can be further related to the passive linewidth of the *Fabry-Perot* cavity $\Delta\nu_c$ *via* the photon lifetime τ_c in the cavity and the power P_m emitted in the cavity mode, where

$$\tau_c = \frac{1}{2\pi\Delta\nu_c} = \left(\frac{n_l' L}{c}\right)\left[\gamma L + \frac{1}{2}\ln\left(\frac{1}{R_1 R_2}\right)\right]^{-1} \tag{2.32}$$

and

$$P_m = \left[\frac{\gamma L + \frac{1}{2}\ln\left(\frac{1}{R_1 R_2}\right)}{\frac{1}{2}\ln\left(\frac{1}{R_1 R_2}\right)}\right] P_o. \tag{2.33}$$

Thus, Eq. (2.31) for $\Delta\nu_{S-T}$ can be rewritten in the form

$$\Delta\nu_{S-T}(\lambda_l) = \frac{\pi hc}{\lambda_l P_m}(\Delta\nu_c)^2 n_{sp}. \tag{2.34}$$

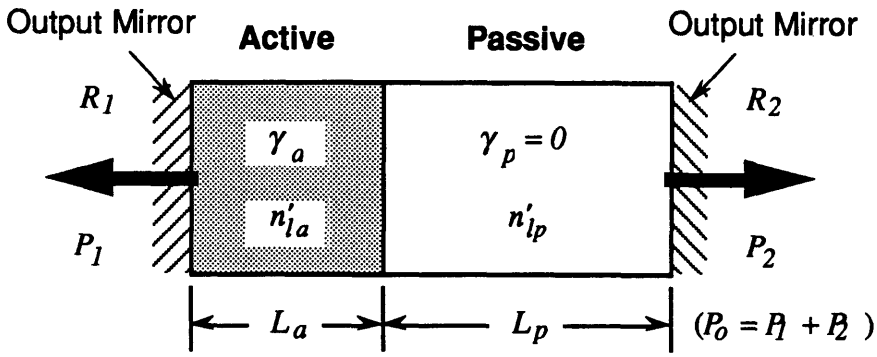

Fig. 2.2 A schematic of a laser with a composite cavity.

In terms of the passive linewidth of the *Fabry-Perot* cavity $\Delta\nu_c$ or the photon cavity lifetime τ_c as given by Eq. (2.32), significant reduction of the *Schawlow-Townes* $\Delta\nu_{S\text{-}T}$ linewidth can be achieved by placing the laser medium in an external cavity. To illustrate the cavity-length dependence of $\Delta\nu_{S\text{-}T}$, consider a laser with a composite cavity, as shown in Fig. 2.2, consisting of an active (gain) medium of length L_a and a passive (zero gain) medium of length L_p contained in series within two mirrors with reflectances R_1 and R_2, respectively. The total output power P_o is the sum of the two output powers P_1 and P_2 emitted from the two output mirrors separately. n'_{l_a} and γ_a are the real part of the refractive index and the internal loss coefficient of the active medium respectively, and n'_{l_p} is the real part of the refractive index of the passive medium which is assumed to be loss-free ($\gamma_p = 0$).

The generalized photon lifetime in this composite cavity becomes

$$\tau_c = \frac{1}{2\pi\Delta\nu_c} = \left(\frac{n'_{l_a}L_a + n'_{l_p}L_p}{c}\right)\left[\gamma_a L_a + \frac{1}{2}\ln\left(\frac{1}{R_1R_2}\right)\right]^{-1}. \qquad (2.35)$$

Subsequently, combining Eq. (2.35) for τ_c and hence for $\Delta\nu_c$ with Eq. (2.33) for P_m, Eq. (2.34) for the *Shawlow-Townes* linewidth $\Delta\nu_{S\text{-}T}$ can be extended to a generalized form

$$\Delta\nu_{S-T}(\lambda_l) = \frac{hc}{8\pi P_o \lambda_l}\left(\frac{c}{n'_{l_a}L_a + n'_{l_p}L_p}\right)^2\left[\gamma_a L_a + \frac{1}{2}\ln\left(\frac{1}{R_1R_2}\right)\right]\ln\left(\frac{1}{R_1R_2}\right)n_{sp}. \tag{2.36}$$

It is obvious that Eq. (2.36) for the modified *Shawlow-Townes* linewidth $\Delta\nu_{S\text{-}T}$ possesses three features: (i) $\Delta\nu_{S\text{-}T}$ is inversely proportional to the total output power P_o, (ii) $\Delta\nu_{S\text{-}T}$ is inversely proportional to the square of the cavity optical-path-length (n_aL_a + n_pL_p), and (iii) $\Delta\nu_{S\text{-}T}$ is inversely proportional to the laser wavelength λ_l. Besides, recall that the linewidth is *Lorentzian* as shown in Eq. (2.20).

For a semiconductor laser, the first feature was first confirmed by *Welford* and *Mooradian*.[4,11] From their observed linewidth, however, they found an unexpected component $\Delta\nu_{PI}$ which is the non-zero extrapolated value for the linewidth at infinite output power and is hence referred to as the power-independent linewidth. Although the nature of $\Delta\nu_{PI}$ is not well understood, their phenomenological model of the effects of statistical carrier number fluctuations appears to be in excellent agreement with the observed magnitude of $\Delta\nu_{PI}$ at *273, 195, 77,* and *1.7* $^{\circ}K$.[12]

The second feature of $\Delta\nu_{S\text{-}T}$ has been applied to reduce linewidth by using external cavity configuration in laser design. Significant linewidth reduction was successfully demonstrated by *Fleming* and *Mooradian,*[13,14] but they could not properly determine the narrowed linewidth because of the resolution limit of their *Fabry-Perot* interferometer. However, they first presented the *Lorentzian* linewidth for a semiconductor laser and revealed the fact that the observed linewidth is significantly broader than that predicted by the modified *Shawlow-Townes* linewidth $\Delta\nu_{S\text{-}T}$ as given by Eq. (2.36). This discrepancy in magnitude attracted attention to the role of the neglected amplitude noise caused by spontaneous emission. Recall that the modified *Shawlow-*

Townes linewidth $\Delta\nu_{S\text{-}T}$ is the result of the instantaneous phase noise caused by spontaneous emission. When the instantaneous amplitude noise is taken into account, a delayed phase noise is induced due to amplitude-phase coupling. The delayed phase noise results in linewidth broadening and is discussed in the following section.

2.2 Power-Dependent Linewidth due to Amplitude Noise

The second term on the right hand side for the electric field of laser radiation as given in Eq. (2.1), represents amplitude noise and was ignored in the derivation of the modified *Schawlow-Townes* linewidth. However, this amplitude noise may lead to additional phase noise; this process is denoted as amplitude-phase (*AM-FM*) coupling. The measure of this coupling is denoted by α. This additional phase noise, sometimes referred to as delayed phase noise, contributes an additional component, proportional to α^2, to the intrinsic linewidth.

Following *Henry*'s[3] analysis, the total phase change $\Delta\varphi_i$ due to the i^{th} spontaneous emission event is the sum of the two terms:

$$\Delta\varphi_i = \Delta\varphi_i' + \Delta\varphi_i'', \tag{2.37}$$

where $\Delta\varphi_i'$ is the instantaneous phase change, as given by Eq. (2.9), caused by spontaneous emission, and $\Delta\varphi_i''$ is the delayed phase change coupled from the instantaneous intensity change ΔI_i, as given by Eq. (2.8), caused by the same spontaneous emission. This, in turn, requires a relation between the rate of change of phase and amplitude to obtain $\Delta\varphi_i''$. Then, the *Gaussian* statistics process that derives the linewidth from $\Delta\varphi_i'$ in Section 2.2 can be applied to $\Delta\varphi_i''$.

As shown in *Henry*'s work[2], the intensity-phase derivative equation is given by

$$\frac{\partial \varphi}{\partial t} = \left(\frac{\alpha}{2I}\right)\frac{\partial I}{\partial t}, \tag{2.38}$$

where

$$\alpha \equiv -\frac{\partial n_l'/\partial N}{\partial n_l''/\partial N} \approx -\frac{\Delta n_l'}{\Delta n_l''}. \tag{2.39}$$

Because the intensity fluctuation is negligible compared to its steady-state value I_o, the variable I in the denominator of Eq. (2.38) can be treated as constant. With the initial ($t_i = 0$) and boundary ($t_i \rightarrow \infty$) conditions for I:

$$I(0) = I_o + \Delta I_i \tag{2.40}$$

$$I(\infty) = I_o, \tag{2.41}$$

the delayed phase change $\Delta\varphi_i''$ accumulated during the post-emission relaxation oscillations that returns the laser intensity from $I(0)$ to $I(\infty)$ is found by integrating Eq. (2.38) from $t_i = 0$ to $t_i = \infty$

$$\Delta\varphi_i'' = -\left(\frac{\alpha}{2I_o}\right)\Delta I_i. \tag{2.42}$$

Substituting for ΔI_i from Eq. (2.8), Eq.(2.41) for the delayed phase change $\Delta\varphi_i''$ is obtained in the form

$$\Delta\varphi_i'' = -\left(\frac{\alpha}{2I_o}\right)\left[I + 2\sqrt{I}\cos\theta_i\right]$$

$$\equiv -\frac{\alpha}{2I} - \left(\frac{\alpha}{\sqrt{I}}\right)\cos\theta_i. \tag{2.43}$$

Combining Eq. (2.43) for $\Delta\varphi_i''$ with Eq. (2.9) for $\Delta\varphi_i'$, the total phase change $\Delta\varphi_i$ in Eq. (2.37) is given by

$$\Delta\varphi_i = \Delta\varphi_i' + \Delta\varphi_i'' = -\frac{\alpha}{2I} - \left(\frac{1}{\sqrt{I}}\right)[\sin\theta_i - \alpha\cos\theta_i]. \tag{2.44}$$

The first term is a small but constant phase change for each spontaneous emission event. Over a large time interval τ, it will yield an average total phase change

$$\langle\Delta\varphi\rangle = \lim_{R_{sp}|\tau|\to\infty} \sum_{i=1}^{R_{sp}|\tau|} \left(-\frac{\alpha}{2I}\right) = -\frac{\alpha R_{sp}|\tau|}{2I}, \tag{2.45}$$

or an angular frequency shift

$$\Delta\omega = \frac{\partial\langle\Delta\varphi\rangle}{\partial t} = -\frac{\alpha R_{sp}}{2I}, \tag{2.46}$$

where R_{sp} is the spontaneous emission rate per cavity mode. Because this constant frequency shift does not affect the linewidth, the first term on the right hand side of Eq. (2.44) can be ignored.

With the effective total phase change $\Delta\varphi_i$ in the form of

$$\Delta\varphi_i = -\left(\frac{1}{\sqrt{I}}\right)[\sin\theta_i - \alpha\cos\theta_i], \tag{2.47}$$

the total intrinsic linewidth can be derived by following Eqs.(2.15) through (2.23) regarding the *Gaussian* statistics. Similar to Eq. (2.22), the value of $\langle\Delta\varphi^2\rangle$ is

$$\langle\Delta\varphi^2\rangle = \frac{R_{sp}|\tau|}{2I}(1+\alpha^2). \tag{2.48}$$

In comparison with Eq. (2.22), the extra scaling factor $(1 + \alpha^2)$ above predicts the enhancement effect for the following parameters. Substituting Eq. (2.48) for $\langle \Delta\varphi^2 \rangle$ into Eq. (2.17), the phase diffusion coefficient D becomes

$$D = \frac{\langle \Delta\varphi^2 \rangle}{2|\tau|} = \frac{R_{sp}}{4I}\left(1+\alpha^2\right). \tag{2.49}$$

The total intrinsic linewidth (*FWHM*) $\Delta\nu$ is also broadened, relative to the modified *Schawlow-Townes* linewidth $\Delta\nu_{S\text{-}T}$, by the same factor

$$\begin{aligned} \Delta\nu &= \frac{D}{\pi} = \frac{R_{sp}}{4\pi I}\left(1+\alpha^2\right) \\ &= \Delta\nu_{S-T}\left(1+\alpha^2\right). \end{aligned} \tag{2.50}$$

Therefore, in the presence of the amplitude-phase coupling, the characteristics associated with the *Schawlow-Townes* linewidth $\Delta\nu_{S\text{-}T}$ are all preserved except in magnitude by a factor of $(1 + \alpha^2)$.

It can be shown that α can be expressed in the form as given by

$$\alpha \equiv -\frac{\partial n_l'/\partial N}{\partial n_l''/\partial N} \approx -\frac{\partial \chi_l'/\partial N}{\partial \chi_l''/\partial N} \approx -\frac{\Delta\chi_l'}{\Delta\chi_l''}, \tag{2.51}$$

where χ_l' and χ_l'' are, respectively, the real and the imaginary parts of the electric susceptibility of the laser medium. The dispersion of χ_l' and χ_l'' for population inversion densities N and $N + \Delta N$ is illustrated in Fig. 2.3 for gas and solid-state lasers, and semiconductor lasers. For a gas or solid-state laser, the lasing transition takes place between two discrete energy levels. As shown in Fig. 2.3(a), this results in a symmetric $\chi_l''(\lambda)$ and an anti-symmetric $\chi_l'(\lambda)$ with respect to the resonant frequency ν_r which corresponds to the energy difference between the two levels. Because lasing transition

tends to occur at the resonant frequency ν_r where the gain ($\propto \chi_l''$) is maximum, it is seen that χ_l' does not change at this particular frequency. This indicates the vanishment of the amplitude-phase coupling at ν_r where the amplitude-phase coupling factor α is zero. Consequently, no linewidth enhancement is expected at the resonant frequency for gas and solid-state lasers.

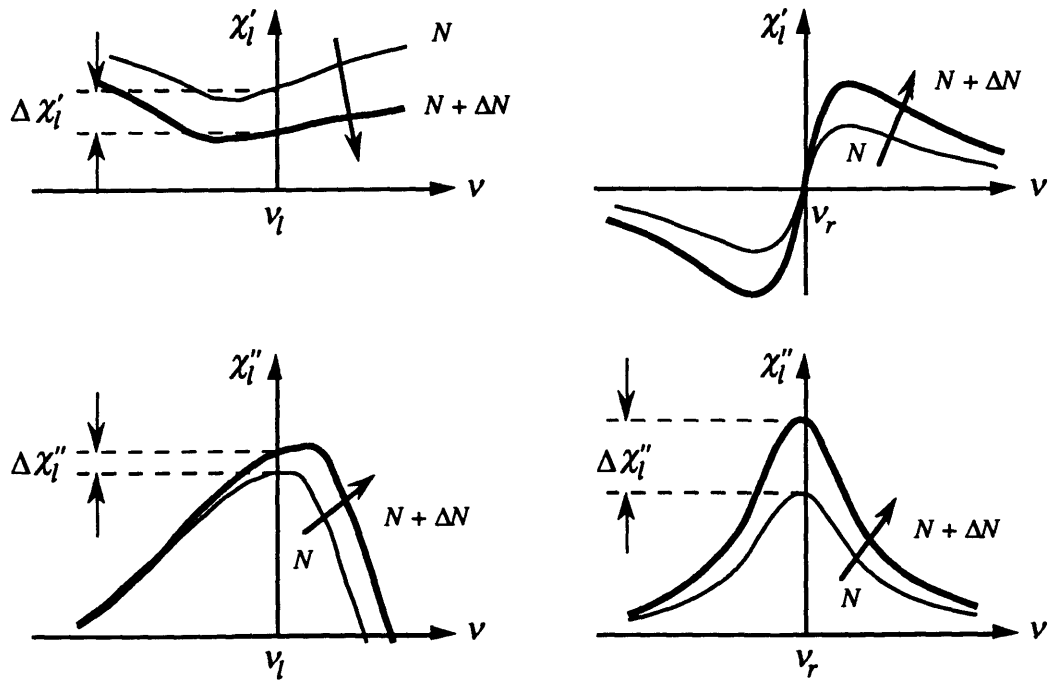

(a) Semiconductor Lasers (b) Gas and Solid-State Lasers

Fig. 2.3 Dispersion of real part χ_l' and imaginary part χ_l'' of the electric susceptibility for (a) a semiconductor laser, and (b) a gas or solid-state laser.

For semiconductor lasers, however, the lasing transition occurs between two energy bands, which leads to dispersion asymmetry of χ_l' and χ_l''.[15,16] As shown in Fig. 2.3 (a), the variation of population inversion density N not only shifts the gain peak in frequency but also changes the magnitudes of χ_l' and χ_l'' at any frequency. This

indicates the existence of the amplitude-phase coupling all over the frequency region where lasing transitions are allowed. Consequently, the amplitude-phase coupling factor α is finite and linewidth enhancement is expected in semiconductor lasers.

By examining Eq. (2.50) for the overall intrinsic linewidth $\Delta\nu$ and Eq. (2.34) for the modified *Schawlow-Townes* linewidth $\Delta\nu_{S\text{-}T}$, the wavelength dependence of the linewidth $\Delta\nu$ is determined by that of α within a few percent of tuning range. A model for the calculation of α as a function of wavelength will be discussed in the next Chapter.

2.3 Power-Dependent Linewidth due to Shot Noise

The shot noise in the carrier population is an additional intrinsic noise source. It contributes to additional power-dependent linewidth and is responsible for the power-independent linewidth $\Delta\nu_{PI}$ as shown in the following analytical expression for the overall intrinsic linewidth $\Delta\nu$:

$$\Delta\nu = \left[\underbrace{\Delta\nu_{S-T}}_{\substack{phase\\ noise}} + \underbrace{\Delta\nu_{S-T}\alpha^2}_{\substack{amplitude\\ noise}} + \underbrace{\left(\Delta\nu_{S-T}\alpha^2\right)f}_{\substack{shot\\ noise}} \right] + \underbrace{\Delta\nu_{PI}}_{\substack{shot\\ noise}}, \tag{2.52}$$

with

$$f \equiv \frac{\Delta\eta_{stat}}{\Delta\nu_{sp}} = \frac{\textit{statistical fluctuations in the carrier population (shot noise)}}{\textit{fluctuations in the carrier population caused by spontaneous emission}}. \tag{2.53}$$

where the [ ] bracket contains the power-dependent components due to phase noise, amplitude noise, and shot noise, respectively, and f as defined in Eq. (2.53) is equivalent

to the ratio of the power-dependent linewidth due to shot noise to the linewidth due to amplitude noise.

The transformation from shot noise to spectral linewidth is through the following steps. The power-dependent linewidth, the fluctuations in the carrier population due to shot noise is converted to fluctuations in amplitude (intensity). The amplitude (intensity) fluctuations are then transformed to spectral linewidth through two series of channels: the *AM-FM* coupling firstly and the phase-linewidth transformation secondly. For this reason, the product of $\left(1+\alpha^2\right)$ and $\Delta\nu_{S-T}$ is a common factor in the power-dependent linewidth caused by shot noise. The factor f as defined in Eq. (5.53) quantifies the fluctuations in the carrier population due to shot noise in terms of that due to amplitude noise caused by spontaneous emission.

The fluctuations in the carrier population $\Delta\eta_{sp}$ caused by spontaneous emission is given by the following general form

$$\Delta\eta_{sp}=\left(\frac{R_{sp}}{\Gamma_s}\right)\tau_{sp}=\left(\frac{\tau_{sp}}{\Gamma_s}\right)\left(\frac{c}{n_{i_a}'L_a+n_{i_p}'L_p}\right)\left[\gamma_a L_a+\frac{1}{2}\ln\left(\frac{1}{R_1R_2}\right)\right], \qquad (2.54)$$

where R_{sp} is the effective spontaneous emission rate (per mode), $0\le\Gamma_s\le 1$ is the optical confinement factor as will be discussed in Section 3.2, τ_{sp} is the carrier lifetime due to spontaneous emission, and the remaining parameters are as shown in Fig. 2.2 for an composite cavity laser. Here $\left(\frac{R_{sp}}{\Gamma_s}\right)$ gives the bulk spontaneous emission rate.

The statistical fluctuations in the carrier population $\Delta\eta_{stat}$ caused by shot noise only depends on the total number of carrier population η_{stat} and is given by

$$\Delta\eta_{stat}=\sqrt{\eta_{stat}}, \qquad (2.55)$$

with

$$\eta_{stat} = VN_{th}, \tag{2.56}$$

where V is the volume of the active medium and N_{th} is the carrier population density at threshold. Consequently, the ratio of the statistical fluctuations to the spontaneous emission fluctuations is given by

$$f \equiv \frac{\Delta\eta_{stat}}{\Delta\nu_{sp}} = \left\{\left(\frac{\tau_{sp}}{\Gamma_s}\right)\left(\frac{c}{n'_{la}L_a + n'_{lp}L_p}\right)\left[\gamma_a L_a + \frac{1}{2}\ln\left(\frac{1}{R_1R_2}\right)\right]\right\}^{-1}\sqrt{\eta_{stat}}. \tag{2.57}$$

For the power-independent linewidth $\Delta\nu_{PI}$, we adopt *Welford* and *Mooradian*'s phenomenological model.[4] In their work on $Al_yGa_{1-y}As$ free-running lasers, they interpreted $\Delta\nu_{PI}$ as due to statistical fluctuations in the carrier population $\Delta\eta_{stat}$ as given by Eq. (2.55), through the fluctuations in the cavity frequency. They deduced

$$|\Delta\nu_{PI}| = \Gamma_s\nu_l\left(\frac{L_a}{n'_{la}|_g L_a + n'_{lp}L_p}\right)\left[\frac{d\left(n'_{la}|_g\right)}{d(\eta_{th})}\right]\Delta\eta_{stat}. \tag{2.58}$$

Here we simply replace the phase refractive index n'_{la} with the group refractive index $n'_{la}|_g$ to account for the dispersion and extend their expression for solitary diode laser to this general form for a composite diode laser and result in the scaling factor $\left(\frac{L_a}{n'_{la}|_g L_a + n'_{lp}L_p}\right)$. In comparison with Eq. (2.36) for the power-dependent *Schawlow-Townes* linewidth $\Delta\nu_{S-T}$ in which the scaling factor decreases with the increasing optical-cavity-length to the second power, therefore, $\Delta\nu_{PI}$ is expected to present relatively less linewidth reduction in an external-cavity diode laser.

CHAPTER 3

SIMPLE INTERBAND MODEL FOR THE CALCULATION OF AMPLITUDE-PHASE COUPLING FACTOR α

The amplitude-phase coupling factor α is an important parameter in the study of wavelength dependence of spectral linewidth. As discussed in Chapter 2, the amplitude-phase (*AM-FM*) coupling involves the real and imaginary parts of the complex susceptibility χ_l. Because χ_l depends upon the band structure of semiconductor and the physical structure of the device, effects of alloy composition, strain due to lattice mismatch, graded-index separated-confinement heterostructure (*GRINSCH*) quantum well structure, and polarization relaxation time T_2 are considered in a simple interband model for the calculation of α in this work. This model neglects the effects of band nonparabolicity, band-tail states, relaxation of momentum conservation for optical transitions, and excitonic and nonradiative recombination.

3.1 Band Structure of Semiconductor

Fig. 3.1(a) shows a typical parabolic energy-band-structure, i.e. electron energy E versus the wavevector k curves for a bulk (3-dimensional) III-V binary or ternary semiconductor such as $In_xGa_{1-x}As$. The most significant parameters are the energy band gap $E_g(x)$ and the effective masses of electron $m_e(x)$ in the conduction band and of the heavy hole (*HH*), $m_{HH}(x)$ and of light hole (*LH*) $m_{LH}(x)$ in the valence bands; they vary with different binary materials and the alloy composition x of the ternary compound. The effective masses are implicitly determined from the curvatures of bands according to

$$m_j = \hbar^2 \left(\frac{\partial^2 E_j}{\partial k_j^2} \right)^{-1}, \tag{3.1}$$

with

$$E_j(k_j) = \frac{\hbar^2 k_j^2}{2m_j}, \tag{3.2}$$

where the subscript j denotes the carriers: electron, HH, or LH, and E_j is the energy of carrier j above the band edge associated with a given state k_j. Note that hole is a virtual carrier which indicates the absence of electron in an allowed state.

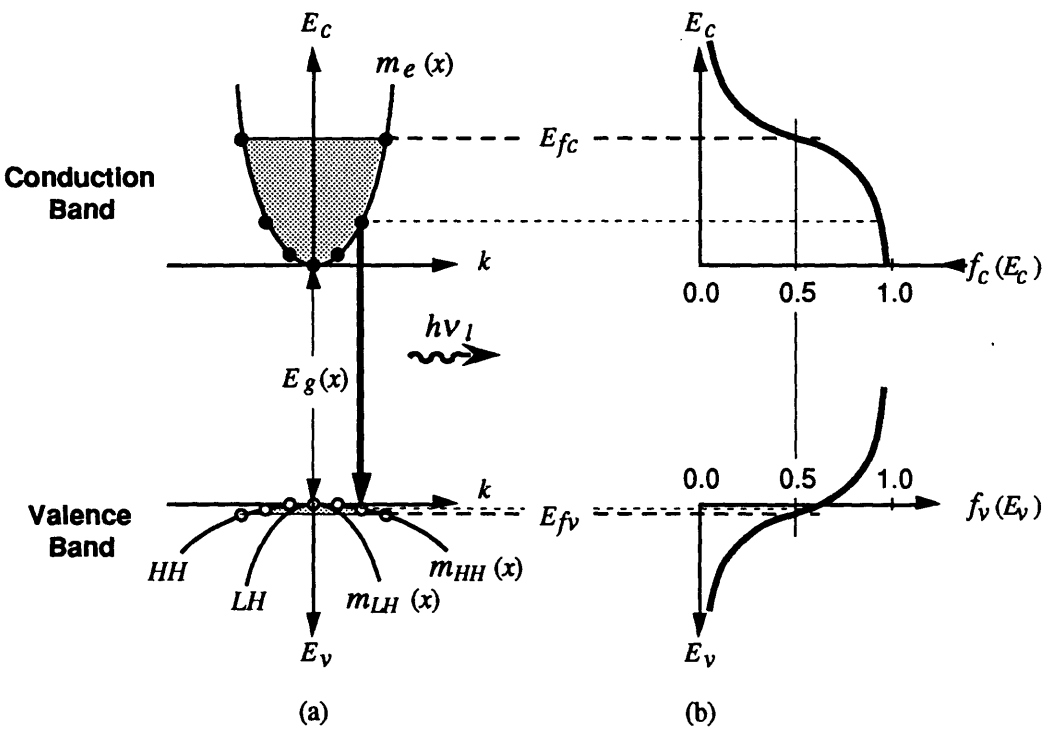

Fig. 3.1 (a) A typical energy band structure for a III-V semiconductor, and (b) Quasi-*Fermi* energies and *Fermi-Dirac* occupation factors for electrons and holes.

The black dots represent electrons in the allowed energy states in the conduction band and the white dots represent holes (*HH, LH*) in the allowed energy states in the valence band. Because electrons in semiconductors obey the *Fermi-Dirac* distribution for the occupation of the allowed states, Fig. 3.1 (b) shows the *Fermi-Dirac* occupation factors

$$f_c(E_c) = \frac{1}{e^{(E_c - E_{fc})/kT} + 1} \tag{3.3}$$

for an electron with energy E_c to occupy a state in the conduction band and

$$f_v(E_v) = \frac{1}{e^{(E_v - E_{fv})/kT} + 1}, \tag{3.4}$$

for a hole (*HH* or *LH*) with energy E_v to occupy a state in the valence band, where k is the *Boltzmann*'s constant, T is the temperature of the semiconductor, and E_{fc} and E_{fv} are the quasi-*Fermi* energies for electrons in the conduction band and for holes in the valence bands respectively.

If the material is extremely thin in one or two dimensions, it is referred to as quantum well ($2D$) or quantum wire ($1D$) in contrast to the bulk ($3D$) material. Quantization of energy levels occurs along the direction of the thin dimension. On the other hand, the allowed states are spaced uniformly along other directions as given by

$$k_i = s\frac{2\pi}{l_i}, \tag{3.5}$$

where s in an integer and l_i is the length of the crystal in the i^{th} direction. It can be shown that the density of states $\rho_j(E_j)$ (per unit energy and volume) for carrier j in a quantum-well diode[9] ($2D$) as used in this experiment are a step function as given by

$$\rho_j(E_j) = \sum_{n=1}^{\infty} \frac{m_j}{\pi\hbar^2 L_{QW}} H(E_j - E_{jn}), \tag{3.6}$$

with

$$\hbar = \frac{h}{2\pi}, \tag{3.7}$$

and

$$H(E_j - E_{jn}) = \begin{cases} 1 & \text{for } E_j > E_{jn} \\ 0 & \text{otherwise} \end{cases}, \tag{3.8}$$

where h is the *Plank*'s constant, L_{QW} is the thickness of the quantum well, E_{jn} is the quantized energy-level n for carrier j, and H is the *Heaviside* function. Consequently, the electron density in the conduction band is the integration of the product of the density-of-states $\rho_e(E_c)$ and its *Fermi-Dirac* occupation factor $f_c(E_c)$ over the entire conduction band as given by

$$N_c = \int_0^{\infty} \rho_e(E_c) f_c(E_c)\, dE_c. \tag{3.9}$$

Similarly, the hole density in the valence band is

$$N_v = \int_0^{\infty} \rho_{HH}(E_v) f_v(E_v)\, dE_v + \int_0^{\infty} \rho_{LH}(E_v) f_v(E_v)\, dE_v, \tag{3.10}$$

which is the sum of the densities of *HH* and of *LH*. Because of charge neutrality,

$$N_c = N_v = N. \tag{3.11}$$

It is obvious that the density-of-states $\rho(E)$, the quasi-*Fermi* energy E_f, and the *Fermi-Dirac* occupation factor $f(E)$ arise from the band structure of semiconductors.

When interband transitions take place, the recombination (generation) of electron-hole pairs results in the optical gain (loss) and the variation of refractive index in semiconductor media. The magnitude of gain (loss) and of refractive index depends on the carrier density N. Because the amplitude-phase coupling factor α involves the coupling between gain (loss) and refractive index through the carrier density fluctuation ΔN, all the band structure parameters as described in this section are relevant for the calculation of α.

3.2 Physical Structure of a Quantum-Well Diode Laser with Graded-Index Separate Confinement Heterostructure (*GRINSCH*)

The performance of a laser, especially a semiconductor diode laser, depends not only upon the intrinsic band structure of the laser medium but also upon the physical structure of the laser device. To illustrate this, first consider a quantum-well $In_xGa_{1-x}As$ / $Al_yGa_{1-y}As$ laser diode with *GRINSCH* structure as depicted in Fig. 3.2. Here the alloy compositions x and y, as shown in Fig. 3.2 (a), are the mole fractions of *In* and of *Al* in host *GaAs*. The $In_xGa_{1-x}As/Al_yGa_{1-y}As$ wafer used for the fabrication of the laser diode for this experiment was grown at *Lincoln Laboratory* using metal-organic vapor phase epitaxy (*MOVPE*) technique[17,18] with a strained graded-index separate-confinement heterostructure (*GRINSCH*) single-quantum-well structure. In addition to the p^+-contact layer and the n^+-substrate, this heterostructure consists of the following layers: a *1.8-μm*-thick (L_C) $n\text{-}Al_{0.4}Ga_{0.6}As$ cladding layer ($y_C = 0.4$), a *0.2-μm*-thick (L_{GR}) graded $n\text{-}Al_yGa_{1-y}As$ barrier layer (y_{GR} linearly graded from *0.4* to *0.2*), a *10-nm*-thick (L_{QW}) $In_xGa_{1-x}As$ active layer ($x_{QW} = 0.14$), a *0.2-μm*-thick graded $p\text{-}Al_yGa_{1-y}As$ barrier layer (y_{GR} linearly graded from *0.2* to *0.4*), and a *1.8-μm*-thick $p\text{-}Al_{0.4}Ga_{0.6}As$ cladding

layer. The device is *1-mm* (L_a) long and *20-μm* (w) wide with an internal loss coefficient $\gamma_a = 0.35\ cm^{-1}$. For simplicity, one facet of the diode is high-reflection (*HR*) coated with reflectance $R_{HR} \geq 99.9\%$ and the other facet is anti-reflection (*AR*) coated with reflectance $R_{AR} < 0.1\%$.

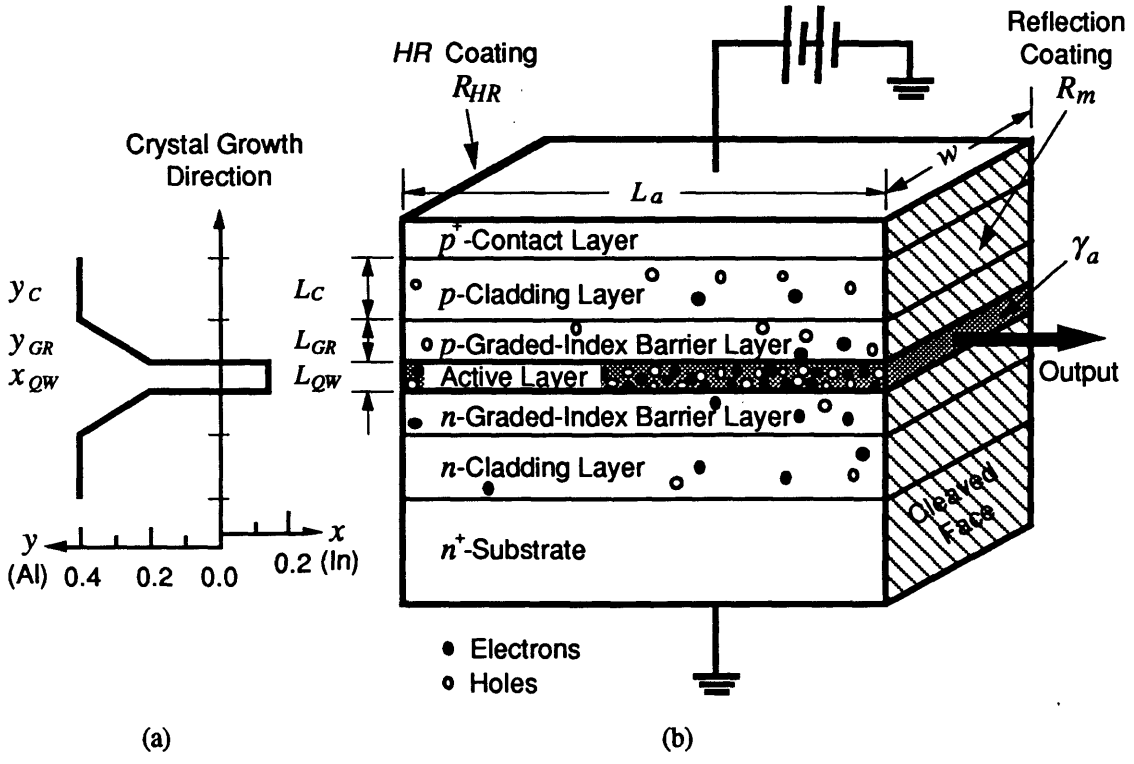

Fig. 3.2 (a) Alloy composition structure along the crystal growth direction, and (b) a typical quantum-well diode laser with *GRINSCH* structure.

When in operation, the diode laser is forward biased. Current injects carriers (electrons and holes) into the diode, which provides the population inversion. The advantage of the heterostructure design is, as shown in Fig. 3.3 (a) to obtain higher population inversion density and waveguiding effect. By forming a potential well in the conduction band to trap the electrons and a potential well in the valence band to trap the holes, a locally higher carrier density is available and laser transitions take place between

the two wells. The formation of the potential wells is implied in Fig. 3.2 (a), because the energy band gap discontinuities (barrier heights) ΔE_c and ΔE_v depend on the alloy compositions x and y. The layer in which the two potential wells are formed for lasing is therefore called the active layer.

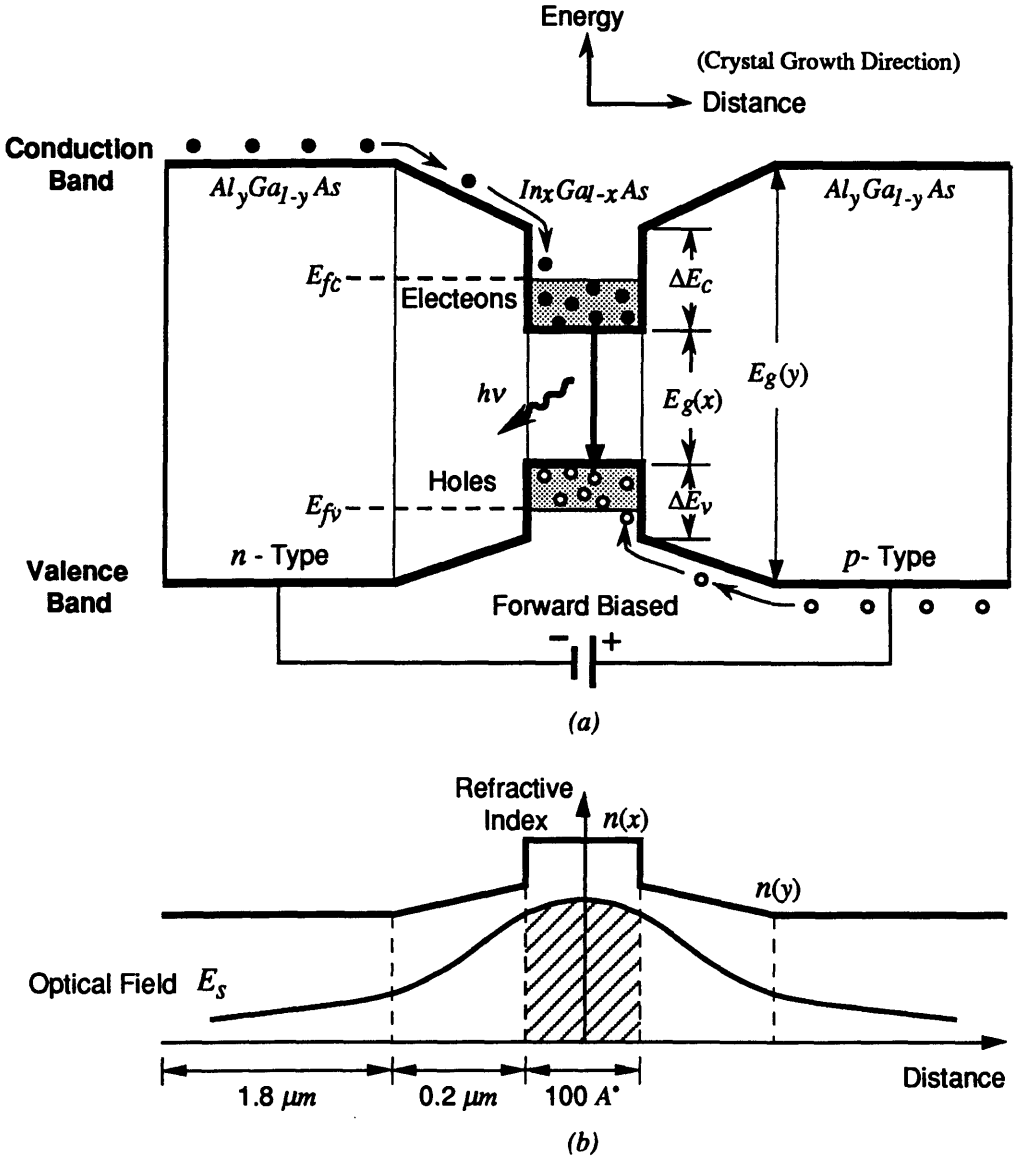

Fig. 3.3 (a) The conduction and valence band edges under forward bias in a quantum-well *GRINSCH* $In_xGa_{1-x}As/Al_yGa_{1-y}As$ laser diode, and (b) The static refractive index profile and the optical field (fundamental mode) profile. Waveguiding effect contributes to the optical energy confinement in the active layer as shaded.

Similarly, the discontinuity in static refractive-index profile leads to an index waveguiding effect: the laser field E_s is stronger in the active layer, as shown in Fig. 3.3 (b), which is the solution of the wave equation for the field under the boundary of the refractive index structure as illustrated. This contributes to the optical energy confinement within the active layer; the ratio of the energy confined in the active layer as shaded to the total energy spread over the layers is defined as the optical confinement factor Γ_s. The product of Γ_s and the bulk gain gives the effective modal gain. This implies that a larger value of Γ_s requires lower injected carrier density for lasing.

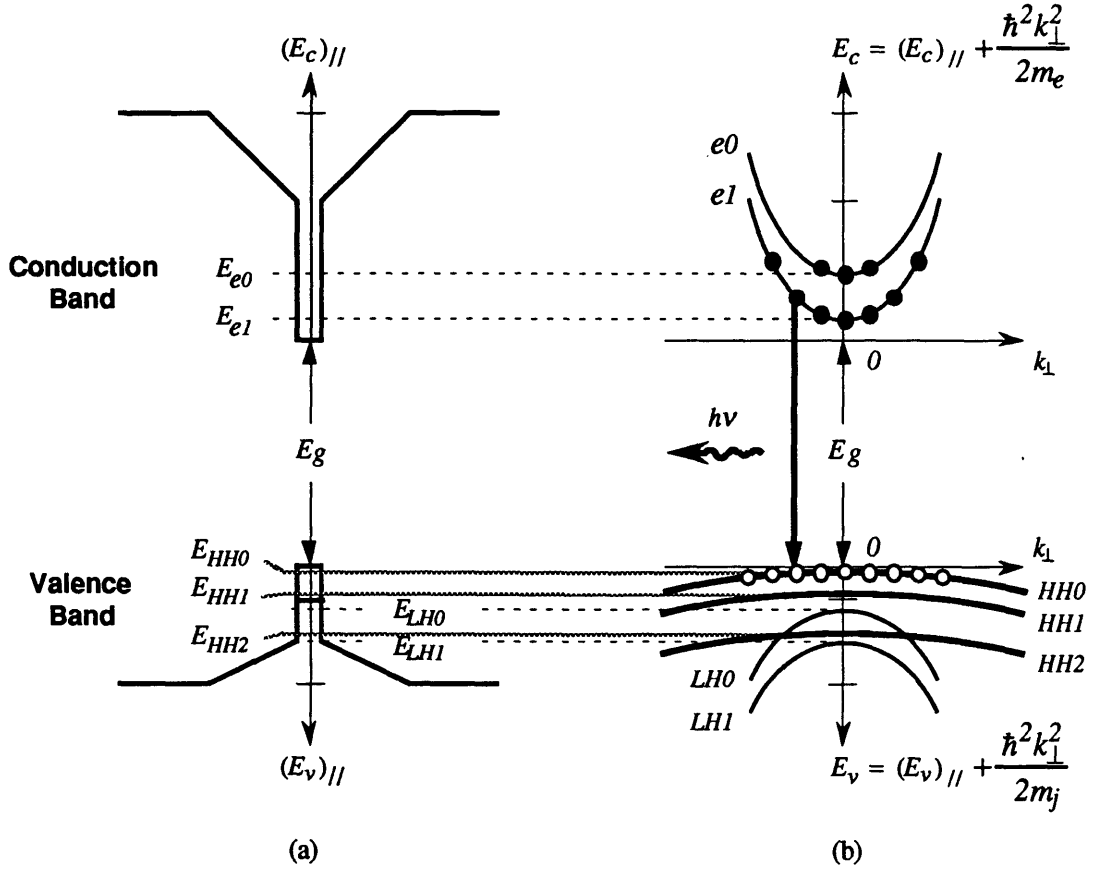

Fig. 3.4 (a) Quantization of the energy levels for electron, *HH* and *LH* in a quantum well, and (b) schematic representation of the parabolic subbands.

As the thickness of the active layer is reduced to the range of hundreds of A°, the confined electrons and holes display quantum effects; their kinetic energies E_{jn} are quantized along this (crystal growth) direction, as shown in Fig. 3.4 (a), where j represents the carrier (electron, *HH*, or, *LH*) and n is the order of the quantized energy level. On the contrary, the kinetic energies in the plane perpendicular to the growth direction remain parabolic with respect to $k_{\perp}$ as given by Eq. (3.2) Therefore, the total kinetic energy for each carrier is, as shown in Fig. 3.4 (b), the sum of the two components as given by

$$E_j = \left(E_j\right)_{//} + \left(E_j\right)_{\perp} = E_{jn} + \frac{\hbar^2 k_{\perp}^2}{2m_j}, \tag{3.12}$$

which leads to subbands. The laser transitions occur between a conduction subband and a *HH* (or *LH*) valence subband of the same order n and releases (absorbs) a photon with energy

$$h\nu_l = E_g + E_c + E_v = E_g + \left(E_{en} + \frac{\hbar^2 k_{\perp}^2}{2m_e}\right) + \left(E_{hn} + \frac{\hbar^2 k_{\perp}^2}{2m_h}\right), \tag{3.13}$$

where E_g is the band gap between the two potential wells, E_c and E_v are the kinetic energies, measured from the electron and hole well bottoms in the conduction and valence bands, respectively, and the subscript h represents for either *HH* or *LH*.

The resulting lasers are therefore called quantum-well (*QW*) diode lasers. The major benefit brought about is that the total number of carriers needed to achieve threshold carrier density in the active layer of the *QW* laser is significantly reduced. Consequently, effects of quantum-well and waveguiding due to the physical structure of the laser diode result in higher modal gain and lower threshold current I_{th}, which affects the amplitude-phase coupling factor α for its dependence on the carrier density N ($\propto I$).

3.3 Effects of Alloy Composition and Strain due to Lattice Mismatch

As a thin active layer of a material with a larger (smaller) lattice constant than the cladding layers is grown, the lattice suffers a compression (expansion) in the plane of the active layer to match that of the barrier layers.[9,10,19] In addition, the lattice constant along the crystal growth direction becomes elongated (shortened) in an effort to keep the volume of each unit cell the same, as illustrated in Fig. 3.5 (a).

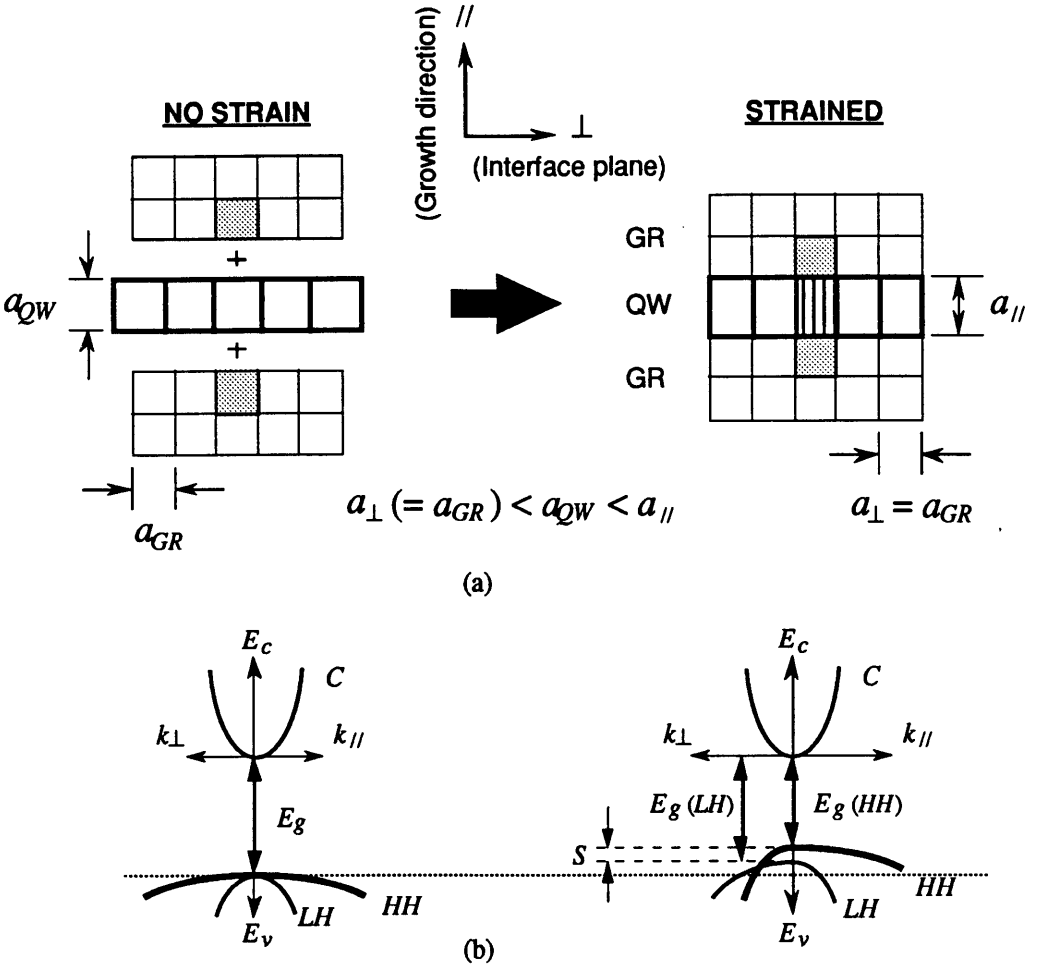

Fig. 3.5 (a) Compressive strain and lattice deformation. Tetragonal distortion due to the application of two-dimensional stress to a cubic crystal. Note that the epitaxial layer contracts in the interfacial plane but expands in the vertical plane, and (b) biaxial strain-induced shift and splitting S of the valence bands.

The distortion in the crystal lattice introduces a deformation perturbation term into the *Schrodinger*-like effective mass equation[20] and results in (a) change in the bandgap of the strained layer,[21-26] (b) separation of the degenerate heavy-hole (*HH*) and light-hole (*LH*) valence bands at $k = 0$,[26,27] and (c) modification of the *HH* and *LH* effective masses.[10,24,27-29] The shift of band gap results in a shift of the laser wavelength. The separation of the *HH* and *LH* bands reduces the band-mixing effect which causes the non-parabolicity of the band structure. This leads to a much lighter *HH* effective mass and slightly heavier *LH* effective mass[30] in the interface plane between the active and barrier layers; the effective masses of *HH* and *LH* along the growth direction remain unchanged. Because the conduction band is relatively far away from the *HH* and *LH* valence bands, the electron effective mass is not affected by the strain perturbation to the first order.[31] The changes in effective masses are reflected in the curvatures of the band structure as shown in Fig. 3.5 (b). A comparison of the effective masses of electron, *HH*, and *LH* in $In_{0.14}Ga_{0.86}As$ in the bulk and the strained quantum well configurations is listed, in the unit of free electron mass m_o, in Table 3.1.

Table 3.1 Effective masses in $In_{0.14}Ga_{0.86}As$ in the bulk and strained quantum well configurations.

	Electron	**Heavy Hole**		**Light Hole**	
	isotropic	in plane$_\perp$	// growth	in plane$_\perp$	// growth
	m_e/m_o	$m_{HH_\perp}/m_o$	$m_{HH_{//}}/m_o$	$m_{LH_\perp}/m_o$	$m_{LH_{//}}/m_o$
Strained	0.061	0.086	0.372	0.176	0.068
Unstrained	0.061	0.372	0.372	0.068	0.068

The reduction of *HH* effective mass due to strain decreases the *HH* density of states. This will raise the quasi-*Fermi* energy and hence the *Fermi-Dirac* occupation factor for *HH* in

the valence band. Consequently, the strain leads to a higher differential gain (gain per injected carrier). This results in lower threshold currents I_{th},[9,10,19] smaller amplitude-phase coupling factor α, and hence narrower linewidth.

Recall that the band structure depends upon the alloy composition, as discussed in Section 3.1. For example, the energy gap E_g for bulk $Al_yGa_{1-y}As$ and $In_xGa_{1-x}As$ is experimentally determined in the form

$$E_g(y) = \begin{cases} 1.424 + 1.247y & \text{for } x > 0.45 \\ 1.424 + 1.247y + 1.147(y - 0.45)^2 & \text{for } x > 0.45 \end{cases} \tag{3.14}$$

and

$$E_g(x) = 1.424 - 1.619x + 0.555x^2. \tag{3.15}$$

In the presence of strain due to lattice mismatch, the material parameters of the strained active layer are modified; the barrier layers remain unstrained. Because laser action occurs in the active layer, Table 3.2 only lists the material parameters for strained $In_xGa_{1-x}As$[32-34] In addition, the lattice constants of the ternary $Al_yGa_{1-y}As$ and the binary $GaAs$ are approximately the same and the strain effect is independent of y. Therefore, these material parameters for strained $In_xGa_{1-x}As$ are given only as a function of x. The *Luttinger* parameters[20] are used to calculated the effective masses of HH and LH, whereas, the spin-orbit energy Δ_{so} is necessary for the calculation of some output parameters such as susceptibility and spontaneous emission rate. The heterostructure discontinuity Q_c, combining $E_g(y)$ given by Eq. (3.14) and $E_g(x)$ listed in Table 3.2, determines the barrier heights of the quantum wells in the conduction and the valence bands for the quantization of energy levels in the wells.

Table 3.2 Material parameters[32,33] for strained $In_xGa_{1-x}As/GaAs$

Description	Function	Unit
Refractive index n_l':	$n_l'(x) = \sqrt{13.18(1-x)+14.6x}$	
Luttinger parameters[20] γ_1 : γ_2 γ_3	$\gamma_1(x) = 6.85(1-x)+3.45x$ $\gamma_2(x) = 2.10(1-x)+0.68x$ $\gamma_3(x) = 2.90(1-x)+1.29x$	$[\hbar^2/m_o]$
Electron effective mass: $m_{c_{//}} = m_{c_\perp} = m_c$	$m_c(x) = 0.067(1-x)+0.15x$	$[m_o]$

Heavy-hole effective mass:
Bulk: $m_{HH_{//}} = m_{HH_\perp} = m_{HH}$
Strained: $m_{HH_\perp} \neq m_{HH_{//}} = m_{HH}$
	$m_{HH}(x) = \hbar^2/[\gamma_1(x)-2\gamma_2(x)]$
	$m_{HH_{//}}(x) = \hbar^2/[\gamma_1(x)-2\gamma_2(x)]$
	$m_{HH_\perp}(x) = \hbar^2/[\gamma_1(x)+\gamma_2(x)]$
		$[m_o]$

Light-hole effective mass:
Bulk: $m_{LH_{//}} = m_{LH_\perp} = m_{LH}$
Strained: $m_{LH_\perp} \neq m_{LH_{//}} = m_{LH}$
	$m_{LH}(x) = \hbar^2/[\gamma_1(x)+2\gamma_2(x)]$
	$m_{LH_{//}}(x) = \hbar^2/[\gamma_1(x)+2\gamma_2(x)]$
	$m_{LH_\perp}(x) = \hbar^2/[\gamma_1(x)-\gamma_2(x)]$
		$[m_o]$

Energy gap E_g	For $x < 0.5$: $E_g(x) = 1.424 - 1.06x + 0.08x^2$ For $1 < x < 0$: $E_g(x) = 1.424 - 1.061x + 0.07x^2 + 0.03x^3$	$[eV]$
Energy splitting S: $S \equiv E_g(LH) - E_g(HH)$	For $x < 0.5$: $S = 0.465x - 0.33x^2$ For $1 < x < 0$: $S = 0.48x - 0.43x^2 + 0.152x^3$	$[eV]$
Spin-orbit split energy Δ_{so}:	$\Delta_{so}(x) = 0.341(1-x)+0.381x$	$[eV]$
Heterostructure discontinuity Q_c: $Q_c \equiv \Delta E_c/\Delta E_g$	$Q_c \equiv \Delta E_c/\Delta E_g = 0.65$ $= \Delta E_c \Big/ \left[E_g(x)\big\|_{QW} - E_g(y)\big\|_{GR} \right]$	

3.4 Input, Intermediate, and Output Parameters

In addition to the material parameters, other parameters used in the calculation are classified into three categories; namely, the input, intermediate, and output parameters. In addition, the carrier density N and vacuum wavelength λ_l are the two variables, and the alloy composition x of the active layer and the polarization relaxation time T_2 are used as the adjustable parameters in this model at room temperature ($20\ ^{\circ}C$).

This model stores the material parameters for strained $In_xGa_{1-x}As$ / $Al_yGa_{1-y}As$ as library functions. The alloy compositions x and y, and the dimensions, the internal loss coefficient, and the effective facet reflectances of the laser device are used as the input parameters of the model to specify the laser diode as listed in Table 3.3.

Table 3.3 Input parameters of the model for the calculation of α.

Description	Symbol	Value
Alloy composition in *QW* layer	x_{QW}	*0.14*
Alloy composition in *GR* layer	y_{GR}	*0.20*
Alloy composition in *C* layer	y_C	*0.40*
Thickness of *QW* layer	L_{QW}	*100 A°*
Thickness of *GR* layer	L_{GR}	*2000 A°*
Thickness of *C* layer	L_C	*18000 A°*
Length of laser diode	L_a	*1 mm*
Width of laser diode	w	*20 μm*
Internal loss coefficient in *QW* layer	γ_a	*3.5 cm^{-1}*
Reflectance on high-reflection *HR* facet	R_{HR}	*100 %*
Effective reflectance on the other facet	R_m	*25 %*
Polarization relaxation time	T_2	*1×10^{-13} sec*

The material parameters such as the energy gaps between conduction band and valence bands, the effective masses of electron and holes, the barrier heights of the two potential wells, and the static refractive indices, as listed in Table 3.2, are first evaluated as a function of the input alloy composition. Subsequently, the two-dimensional intermediate parameters such as density of states, quasi-*Fermi* energies, and the *Fermi-Dirac* occupation factor are calculated. Separately, the one-dimensional intermediate parameters such as quantum-well energy levels and optical confinement factor are calculated by applying *Chinn*'s model[35,36] for diode lasers with *GRINSCH* structure. The related equations and formulae[32-34,37] for the evaluation of these intermediate parameters are given in Table 3.4.

Given the quantized energy levels E_{jn} for carrier j (electron, *HH*, or *LH*) where n is the quantum number of the energy subbands, the following parameters can be calculated for the derivation of the output parameters:

$$E_q = E_g + E_{e0} + E_{HH0}, \tag{3.16}$$

is the lowest energy subband gap,

$$|M_b|^2 = \frac{m_o^2 E_q\left(E_q + \Delta_{so}\right)}{6m_e\left(E_q + 2\Delta_{so}/3\right)}, \tag{3.17}$$

is the momentum matrix element[38] where Δ_{so} is the spin-orbit energy as given in Table 3.2, and

$$\mu = \frac{em_{o\lambda}}{2\pi c} M_b, \tag{3.18}$$

is the electric dipole moment.

Table 3.4 Intermediate Parameters[28-31,37] of the model for the calculation of α

Description	Related Equations or Formulae
Density of state ρ_j for carrier j	$\rho_j(E_j) = \sum_{n=0}^{\infty} \frac{m_{j\perp}}{\pi \hbar^2 L_{QW}} H(E_j - E_{jn})$
Fermi-Dirac distributions: conduction band: f_c valence band: f_v	$f_c(E, E_{fc}) = \frac{1}{e^{(E-E_{fc})/kT} + 1}$ $f_v(E, E_{fv}) = \frac{1}{e^{(E-E_{fv})/kT} + 1}$
Quasi-*Fermi* energy levels: conduction band: E_{fc} valence band: E_{fv}	Total carrier density N in either band: $N_c = \int_0^{\infty} \rho_e(E) f_c(E, E_{fc})\, dE$ $N_c = N_v = N_{v_{HH}} + N_{v_{LH}}$ $N_v = \sum_{HH}^{LH} \left[\int_0^{\infty} \rho_{v_j}(E) f_v(E, E_{fv})\, dE \right]$
Threshold condition: bulk gain $g_{th}\|_{bulk} = \gamma_a - \left(\ln\sqrt{R_{HR}R_m}\right)/L_a$	Threshold condition: modal gain $g_{th}\|_{modal} = \Gamma_s\, g_{th}\|_{bulk}$
Optical confinement factor[36] Γ_s: $\Gamma_s \equiv \int_{\substack{active \\ layer}} dx\, \lvert E_s\rvert^2 \Big/ \int_{\substack{all \\ layers}} dx\, \lvert E_s\rvert^2$	Wave Equation for electric field E_s: $\left[\nabla_z^2 - \left(\frac{n_l'(z)}{c}\right)^2 \frac{\partial^2}{\partial t^2}\right] E_s(z) = 0$
n^{th} Quantized Energy Level[35] E_{jn} for carrier j n *QW:*	*Schrodinger* Equation for energy E_{jn}: $\left[-\frac{\hbar^2}{2m_{j//}^2}\nabla_z^2 + V(z)\right] \psi_n(z) = E_{jn}\, \psi_n(z)$

Using the model of *Dutta*[38] for the quantum well (*QW*) gain and spontaneous radiative recombination rate, the output parameters of the present model in this work are numerically calculated according to the formulae[3,9,10,37] as listed in Table 3.5, where

$$g(\omega) = \frac{T_2}{\pi\left[1+(\omega-\omega_o)^2 T_2^2\right]} \tag{3.19}$$

is the normalized *Lorentzian* lineshape function[39] where T_2 is the polarization relaxation time. The output parameters include the electric susceptibility χ_I, gain g ($\propto \chi''$), amplitude-phase coupling factor α, total spontaneous emission rate per unit volume R_T, spontaneous emission lifetime τ_{sp}, current density J, and current I. In considering the threshold condition, the threshold values of these output parameters are obtained.

Table 3.5 Output parameters of the model for the calculation of α.[3,9,10,37]

1	Susceptibility: $\chi_l(\omega_l) = \chi_l(\omega_l)\big\|_{e-HH} + \chi_l(\omega_l)\big\|_{e-LH}$ $\underset{e-hole}{\chi_l(\omega_l)} = \int_0^{\Delta E_C} dE_c \left\{ \frac{\pi\mu_{hole}^2[(\omega_l - \omega_o)T_2 + i]}{\varepsilon_o \hbar} g(\omega_l) \frac{\rho_{QW_e}(E_c)}{L_{QW}} \left[f_c(E_c) + f_v\left(E_{v_{hole}}\right) - 1 \right] \right\}$
2	Gain $g(\lambda_l)$: $g(\lambda_l) = (2\pi/\lambda_l\, n)\chi_l"(\lambda_l)$
3	Amplitude-phase coupling factor[2] $\alpha(\lambda_l)$: $\alpha(\lambda_l) = -\frac{\partial\chi_l'(\lambda_l)/\partial N}{\partial\chi_l"(\lambda_l)/\partial N} = -\frac{\Delta\chi_l'(\lambda_l)}{\Delta\chi_l"(\lambda_l)}\Big\|_{\Delta N}$
4	Total spontaneous emission rate per unit volume R_T: $[sec^{-1}\ cm^{-3}]$ $R_T \approx R\big\|_{e-HH} + R\big\|_{e-LH}$, where $R\big\|_{e-hole} = \int_0^{\infty} d\lambda_l \left[R(\lambda_l)\big\|_{e-hole} \right]$ and $R(\lambda_l)\big\|_{e-hole} = \int_0^{\infty} dE_c \left\{ \left(\frac{\mu^2 \omega_l^3 n_l'}{\pi c^3 \hbar \varepsilon_o} \right) g(\omega_l) \times \frac{\rho_{QW_e}(E_c)}{L_{QW}} \left[f_c(E_c) + f_v(E_v)\big\|_{hole} - 1 \right] \right\}$
5	Spontaneous emission lifetime τ_{sp}: $[sec]$ $\tau_{sp} = N/R_T$
6	Current density J: $J = q\,N\,L_{QW}/\tau_{sp}$
7	Current I: $I = J\,A = q\,N(L_{QW}\,A)/\tau_{sp} = q\,N\,V/\tau_{sp}$

3.5 Calculated Amplitude-phase coupling factor α and Linewidth Versus Wavelength

The output parameters are computed, using the formulas listed in Table 3.5, as a function of laser wavelength λ_l for various injection carrier densities N at room temperature $T = 293\ ^\circ K$. The most interesting output parameters are the amplitude-phase coupling factor $\alpha(\lambda_l, N)$, and the threshold current $I_{th}(\lambda_l)$. However, the electric susceptibility $\chi_l(\lambda_l, N)$ is necessary for the derivation of $\alpha(\lambda_l, N)$ according to

$$\alpha(\lambda_l) = -\frac{\partial \chi_l'(\lambda_l)/\partial N}{\partial \chi_l''(\lambda_l)/\partial N} = -\frac{\Delta \chi_l'(\lambda_l)}{\Delta \chi_l''(\lambda_l)}\bigg|_{\Delta N}. \tag{3.20}$$

Figs. 3.6 (a) and (b) illustrate $\Delta\chi_l'|_{\Delta N}$ and $\Delta\chi_l''|_{\Delta N}$ *vs.* wavelength at a fixed ΔN. Notice that the imaginary part $\Delta\chi_l''|_{\Delta N}$ falls to zero rapidly within a short range for λ_l beyond *940 nm*, while the real part $\Delta\chi_l'|_{\Delta N}$ remains finite. This feature is expected to result in a sharp rise for $\alpha(\lambda_l, N)$ when λ_l approaches *940 nm* from shorter wavelengths according to Eq. (3.20). As shown in Fig. 3.6 (c), the calculated α increases rapidly with increasing wavelength for $\lambda_l > 940\ nm$; $\alpha = 2.6$ at *940 nm* as a reference. This is because as laser photon energy approaches the band gap of the quantum-well, the gain starts dropping to zero quickly. The active medium needs more and more carrier density N to maintain the threshold gain $g_{th}(\lambda_l)$, which is proportional to χ_l''. Up to a point, the fluctuation of gain g (amplitude) due to spontaneous emission can not be restored no matter how many carriers are driven into the system. However, this large amount of extra carriers induces a big change in χ_l' (phase noise), which results in a rapid increase in α, and, consequently, a large broadening of linewidth.

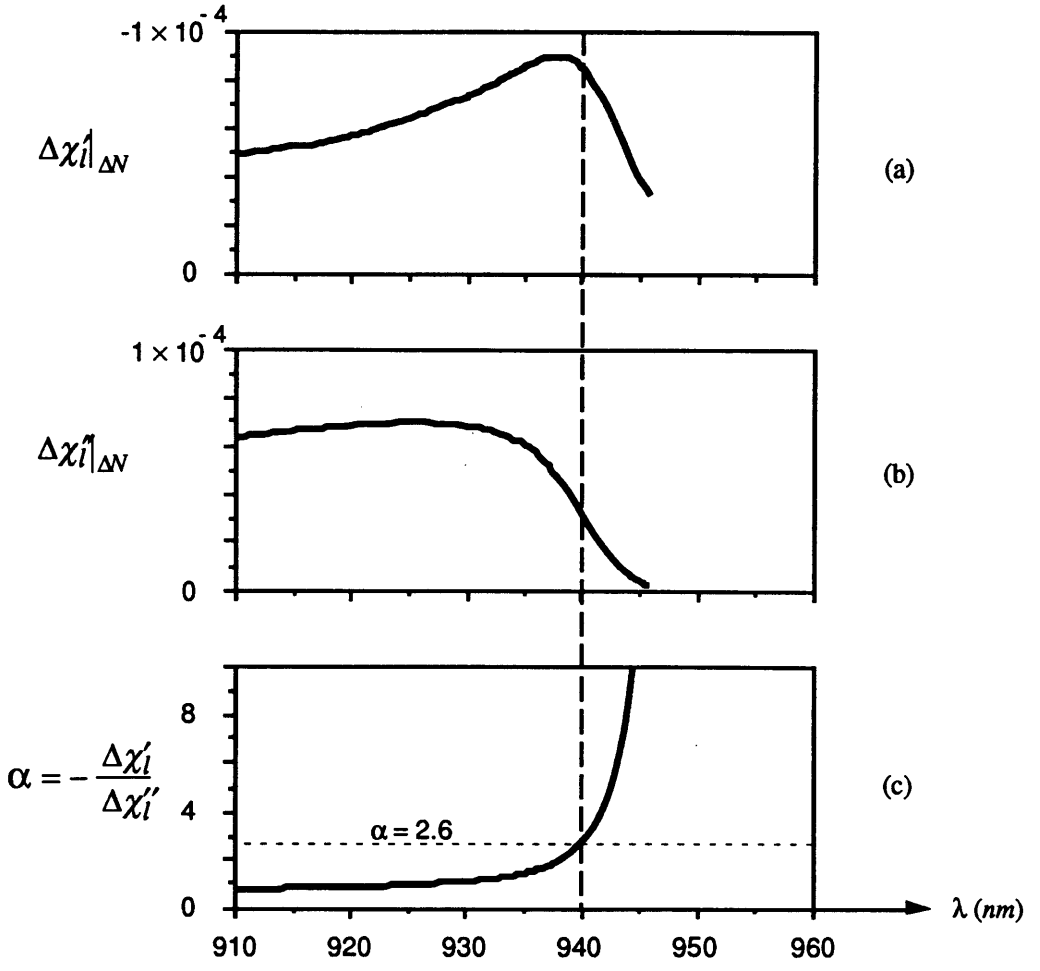

Fig. 3.6 Calculated (a) $\Delta\chi_l'|_{\Delta N}$, (b) $\Delta\chi_l''|_{\Delta N}$, and (c) α as a function of wavelength at threshold condition, using $x = 0.14$ and $T_2 = 1 \times 10^{-13}$ *sec*, and $\Delta N = 1 \times 10^{15}$ cm^{-3}.

Knowing $\alpha(\lambda_l)$, the linewidth $\Delta\nu$ due to spontaneous emission alone can be evaluated according to Eqs. (2.50) for $\Delta\nu$ and (2.36) for the *Schawlow-Townes* linewidth $\Delta\nu_{S-T}$, respectively,

$$\Delta\nu(\lambda_l) = \Delta\nu_{S-T}\left[1+\alpha^2(\lambda_l)\right], \tag{3.21}$$

and

$$\Delta\nu_{S-T}(\lambda_l) = \frac{hc}{8\pi P_o \lambda_l}\left(\frac{c}{n'_{l_a}L_a + n'_{l_p}L_p}\right)^2\left[\gamma_a L_a + \frac{1}{2}\ln\left(\frac{1}{R_1 R_2}\right)\right]\ln\left(\frac{1}{R_1 R_2}\right)n_{sp}. \tag{3.22}$$

Assuming the external-cavity laser is running with an output power $P_o = 5\ mW$ at $\lambda_l = 940nm$, and using the values for the various parameters given in Tables 3.2 and 3.3 $\left(n'_{l_a} = 3.6,\ L_a = 1mm,\ n'_{l_p} = 1,\ L_p = 10cm,\ \gamma_a = 3.5/cm,\ R_1 = R_{HR} \geq 99.9\%,\right.$ $\left.R_2 = R_m \sim 25\%,\text{ and } n_{sp} \sim 1\right)$, Eq. (3.22) for the *Schawlow-Townes* linewidth yields

$$\Delta\nu_{S-T} \cong 20\ Hz. \tag{3.23}$$

Combining Eq. (3.23) for $\Delta\nu_{S-T}$ with $\alpha(\lambda)$ at $x = 0.14$ and $x = 0.16$, Eq. (3.21) for $\Delta\nu(\lambda_l)$ due to spontaneous emission is plotted *versus* wavelength as shown in Fig. 3.7. Both linewidths exhibit the same feature of sharp rise as $\alpha(\lambda_l)$ does except turning at different wavelengths which correspond to different band gaps due to somewhat different x values.

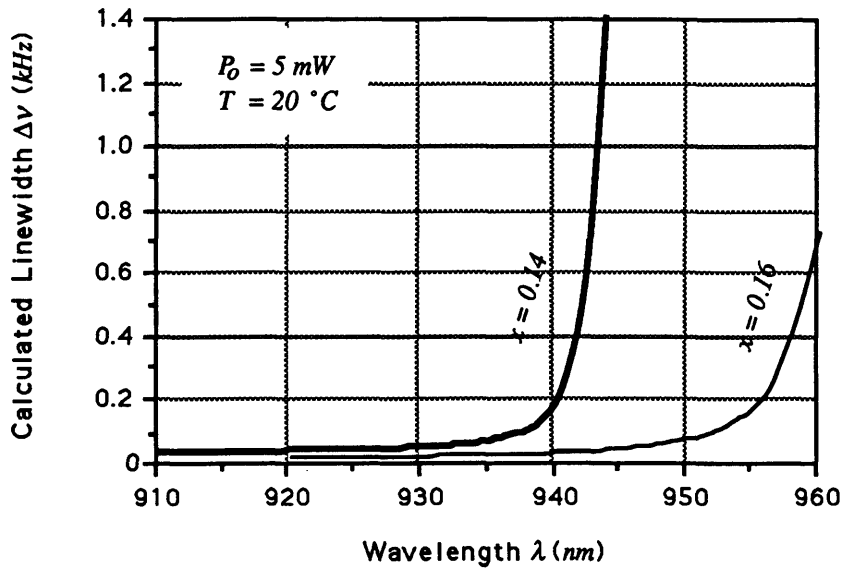

Fig. 3.7 Calculated linewidth due to spontaneous emission alone *versus* wavelength for $x = 0.14$ and $x = 0.16$.

CHAPTER 4

EXPERIMENTAL PROCEDURE

The experimental setup used in this work allows a measurement of the spectral dependence of laser linewidth as a function of wavelength. This work involves (a) the design and construction of two grating-tuned free-running external-cavity diode lasers, and (b) the heterodyne measurement of laser linewidth using these two lasers.

4.1 Design of Grating-Tuned External-Cavity Diode Laser

The use of external cavity provides three advantages: i) broad-band wavelength tunability by using a diffraction grating as a wavelength selector, ii) linewidth reduction due to the increase of photon cavity lifetime, and iii) single-mode operation.[13]

A schematic of the grating-tuned external-cavity diode laser is shown in Fig. 4.1. The system contains a temperature-controlled solitary diode laser, imaging optics, and a blazed grating in a rigid cavity. This strained quantum-well $In_{0.14}Ga_{0.86}As/Al_{0.4}Ga_{0.6}As$ *GRINSCH* laser diode was fabricated at *Lincoln Laboratory*. One facet of this diode laser was high-reflection (*HR*) coated with reflectance $R_{HR} \geq 99.9\%$ and the other facet was anti-reflection (*AR*) coated with $R_{AR} < 0.1\%$. The *HR* coating serves as an end-mirror of the external cavity. The *AR* coating is to avoid the interference between the external cavity and the tiny resonant cavity in the solitary diode.

The *HR/AR* laser diode was mounted on a heat sink which is made of oxygen-free-high-conductivity copper with high thermal conductivity. The temperature of the

heat sink is controlled by a thermal-electric (*TE*) cooler (*Marlow Industries, Inc., Model M1-04002-2*) which is sandwiched between the heat sink and a water block. The TE cooler is controlled by a thermoelectric control unit (*Canadian Instrumentation and Research Limited, Model 902B*). The circulation of chilled water through the water block removes the heat dissipated from the *TE* cooler.

The imaging optics consists of an objective lens, a half-wave plate, and a beam splitter. The polarization of emission is parallel to the interface plane between the active and graded-index layers. The beam diverges from the *AR* coated facet of the diode in the epilayer growth direction rapidly. This diverging light was first collimated by a *Fujinon* objective lens which is a spherically corrected achromat of focal length ~ *0.5 in.* Subsequently, the polarization of this collimated light was rotated by *90* degree through a half-wave plate for a higher diffraction efficiency and resolving power from the grating behind this plate. A *60%*-transmission beam splitter is inserted to couple out two beams in opposite directions.

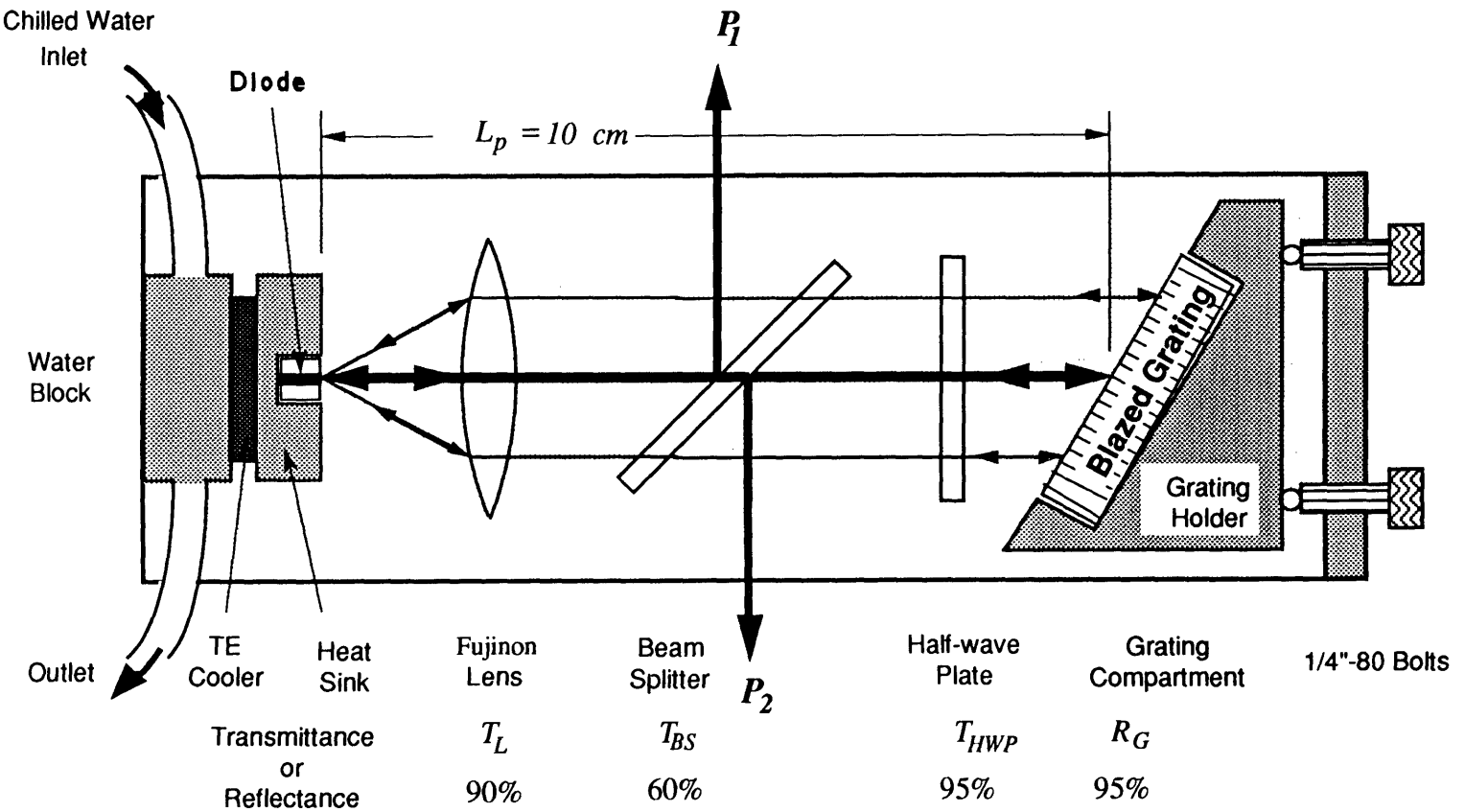

Fig. 4.1 Schematic of the grating-tuned external-cavity diode laser.

The *Littrow*-mounted diffraction grating (*Milton Roy Co.*) is a wavelength selector and served as the second end-mirror of the external cavity. The grating was mounted *10 cm* away from the solitary diode and oriented in the beam diverging direction. As illustrated in Fig. 4.2, the *1.5-cm* wide and *3.75-cm* long blazed grating has *1200* lines per *mm* and a blaze angle $\gamma = 30°$. Using the first order of diffraction, the *1-in*-wide diffracted beam from the grating has a bandwidth $\Delta\nu_G \sim 5.87\ GHz$.

It can be shown that the power reflectance of grating depends upon the polarization of the diffracted beam. Within the tuning range in this experiment, the grating provides higher reflectance for the *p*-polarization, in which the electric field of the light is in the plane of incidence than for the *s*-polarization in which the field is perpendicular to the plane of incidence. This is the reason for the use of a half-wave plate to rotate the polarization of the beam. Measurement showed that the *p*-polarization reflectance of the grating is $R_G \sim 95\%$, the transmittance of the half-wave plate $T_{HWP} \sim 95\%$, the transmittance of the beam splitter $T_{BS} \sim 60\%$, and the transmittance of the *Fujinon* lens $T_L \sim 90\%$. Therefore, the overall reflectance for a round trip is

$$\begin{aligned} R &= R_{HR}\, T_{AR}\, T_L\, T_{BS}\, T_{HWP}\, R_G\, T_{HWP}\, T_{BS}\, T_L\, T_{AR} \\ &= R_{HR}\, R_m, \end{aligned} \tag{4.1}$$

where

$$\begin{aligned} R_m &= T_{AR}\, T_L\, T_{BS}\, T_{HWP}\, R_G\, T_{HWP}\, T_{BS}\, T_L\, T_{AR} \\ &\cong 25\%, \end{aligned} \tag{4.2}$$

is the effective reflectance of a virtual end-mirror of the external cavity.

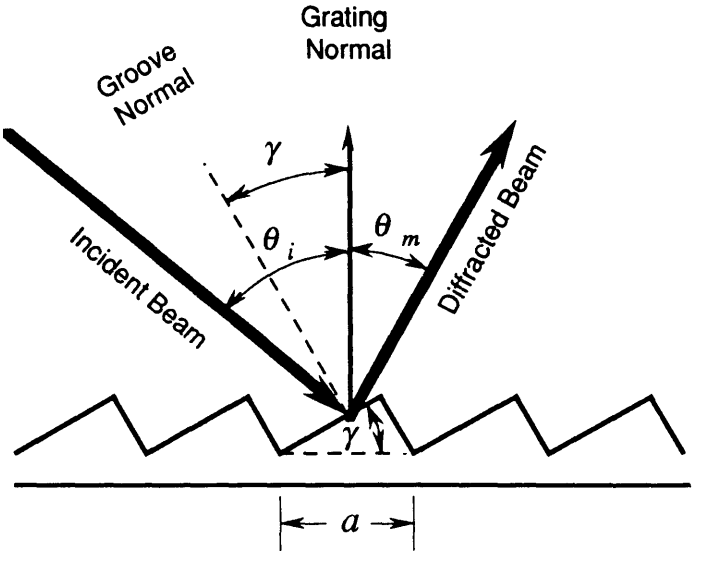

(a)

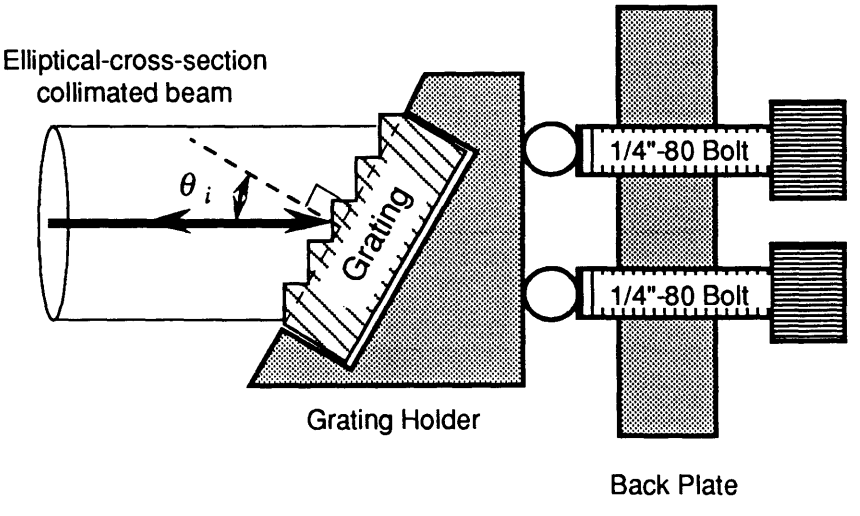

(b)

Fig. 4.2 (a) Section of a blazed grating, and (b) The *Littrow* autocollimation mounting.

Consider a *10-cm*-long effective *Fabry-Perot* cavity consisting of two end mirrors with reflectances $R_{HR} = 99.98\%$ and $R_m, = 25\%$, respectively. The free spectral range ν_{FSR}, which is the longitudinal mode spacing, is

$$\nu_{FSR} = \frac{c}{2\left(n_a L_a + n_p L_p\right)} = \frac{3 \times 10^{10}\, cm/sec}{2(3.6 \times 0.1cm + 1 \times 10cm)} \cong 1.5\ GHz, \qquad (4.3)$$

where c is the speed of light in vacuum, $n_p = 1$ is the refractive index of air, $L_p = 10\ cm$ is the length of the external cavity. In comparison, the bandwidth $\Delta\nu_G \sim 5.87\ GHz$ of the grating covers three to four longitude modes.

In order to reduce the technical vibration noise due to mechanical vibrations of the laser cavity, the major components of the cavity structure were machined from Superinvar with a thermal expansion coefficient $-1.26 \times 10^{-7}\ ^{\circ}C^{-1}$. In order to reduce the technical vibration noise due to other sources of external noise, the two lasers were operated on a laser table. Further acoustic isolation was provided by mounting the lasers on an aluminum plate atop a box of sand and within a plexiglass enclosure, as illustrated in Fig. 4.3.

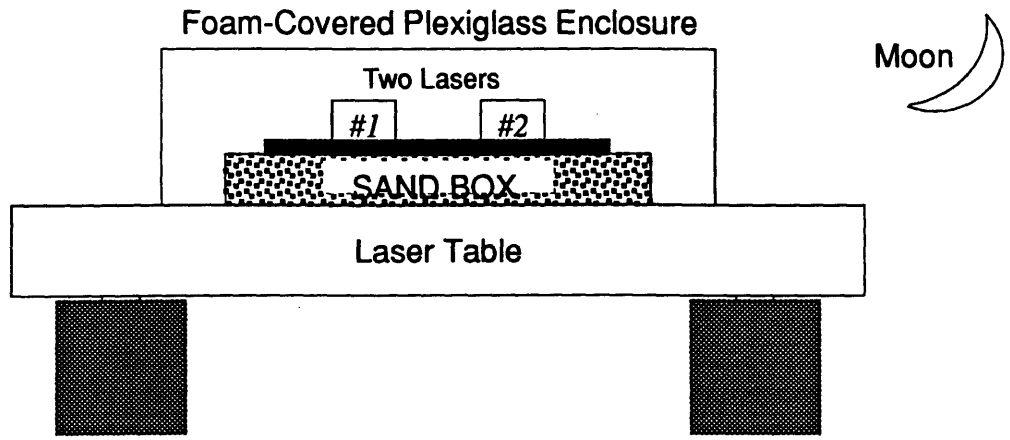

Fig. 4.3 Acoustic isolation arrangement.

4.2 Measurement of the Threshold Current

Current is one of the output parameters which is controllable and measurable. Measuring the output power as a function of current provides a simple technique for determining the threshold current of a laser. Fig. 4.4 shows a block diagram of the setup for the measurement of threshold current. Because of the configuration of the external cavity, there were two output beams from each laser. The weaker beam was focused into a power meter (*Anritsu Optical Power Meter, Model ML 910B* with $\pm 5\%$ accuracy) for the calibration of the total output power. The stronger beam was split by a beam splitter. One of the split beam was sent to a confocal scanning *Fabry-Perot* interferometer (*Coherent Model 240* with *1.5 GHz* free spectral range) to verify single-mode operation. The other split beam was directed into a *0.3-m* and *f/5.3* spectrometer (*McPherson Model 218*) to monitor the coarse wavelength tuning.

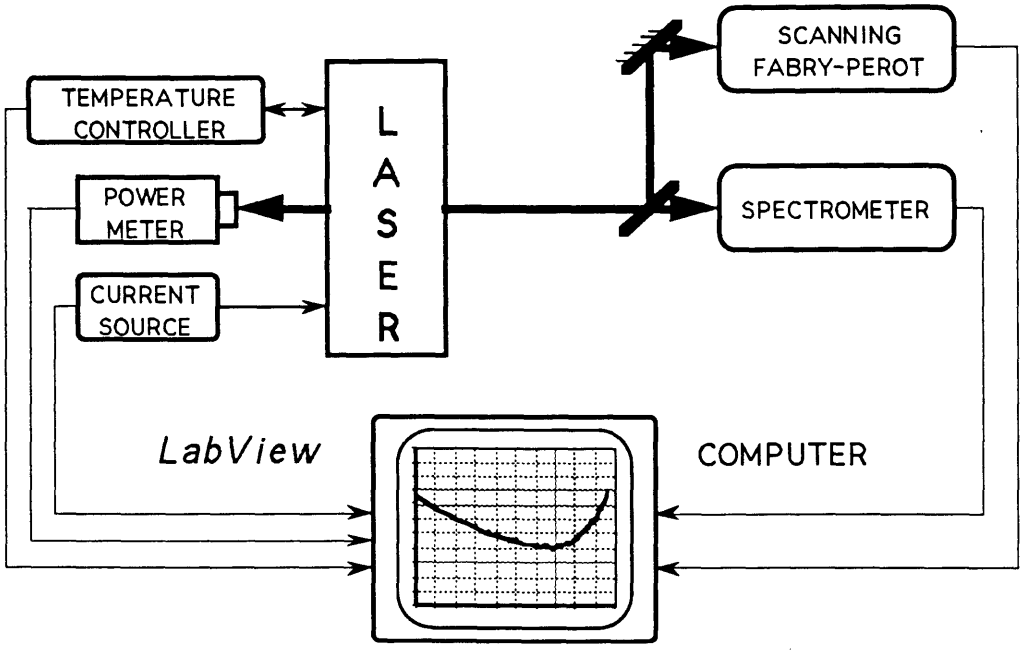

Fig. 4.4 Block diagram of the setup for threshold current measurement.

The values of the total output power and the current were simultaneously recorded and plotted by a *LabView x-y* plotter which is a computer software. The magnitude of the current was adjusted manually. After every plot, the wavelength was tuned *1 nm* up or down by turning the *1/4"-80* fine bolt to change the diffraction angle of the grating. The shift of wavelength was monitored by a video camera in front of the outlet slit of the spectrometer. The resolution of this arrangement is *1 A°*.

Fig 4.5 shows a typical plot of the laser output power *versus* current. The threshold current was determined by extrapolating the sharply rising part of the power-current curve. The intersection of this curve with the current axis was taken as the value of the threshold current. A program performed this evaluation for every power-current curve at different wavelengths. In this manner, a plot of threshold current as a function of wavelength was obtained.

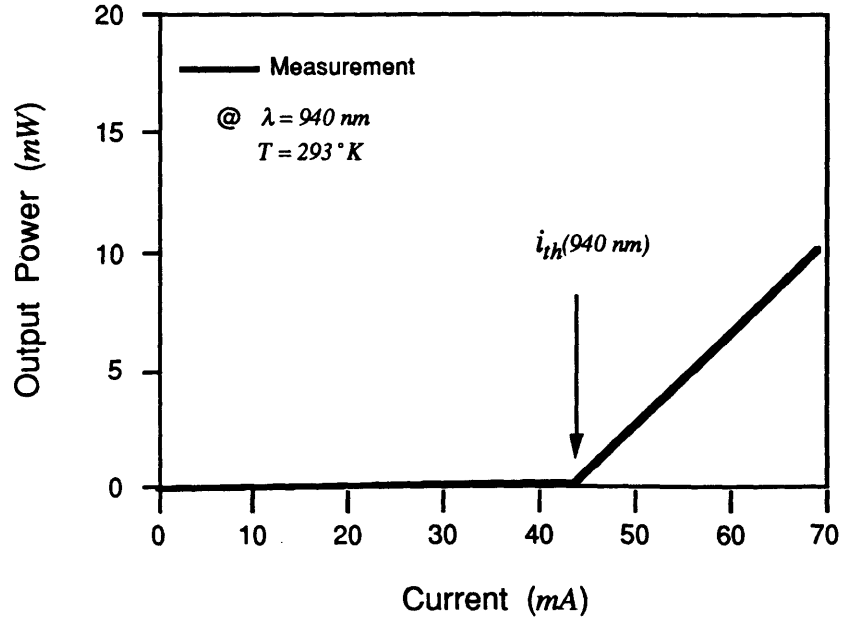

Fig. 4.5 Plot of laser output power as a function of injection current.

4.3 Measurement of the Laser Linewidth using Heterodyne Technique with Two Free-Running Lasers

The external cavity laser linewidth and frequency stability were determined from heterodyne measurements involving two independent, free-running lasers. Suppose the two laser beams are plane wave with electric fields

$$\vec{E}_1(t, x) = \vec{E}_{o_1} \cos\left[2\pi\nu_1 t - k_1 x + \varphi_1(t)\right], \tag{4.4}$$

and

$$\vec{E}_2(t, x) = \vec{E}_{o_2} \cos\left[2\pi\nu_2 t - k_2 x + \varphi_2(t)\right], \tag{4.5}$$

where the subscript *1* or *2* denotes the laser number, and $\vec{E}_{o_i}$, ν_i, k_i, and φ_i are the amplitude, frequency, wavevector, and phase noise of the laser field, respectively. The net field $E(t)$ of the collinear beams is then given by

$$\vec{E}(t) = \vec{E}_{o_1} \cos\left[2\pi\nu_1 t + \varphi_1(t)\right] + \vec{E}_{o_2} \cos\left[2\pi\nu_2 t + \varphi_2(t)\right], \tag{4.6}$$

assuming that the detector is located at $x = 0$. Consequently, the intensity $i_H(t)$ incident on the square-law photodetector is

$$\begin{aligned} i_H(t) &= \vec{E}(t) \bullet \vec{E}(t) \\ &= \frac{E_{o1}^2}{2}\Big[\underbrace{1}_{\substack{D.C.\\ current}} + \underbrace{\cos 2\left(2\pi\nu_1 t + \varphi_1(t)\right)}_{\substack{A.C.\ current\\ in\ optical\ freq.}}\Big] + \frac{E_{o2}^2}{2}\Big[\underbrace{1}_{\substack{D.C.\\ current}} + \underbrace{\cos 2\left(2\pi\nu_2 t + \varphi_2(t)\right)}_{\substack{A.C.\ current\\ in\ optical\ freq.}}\Big] + \\ &\quad \left(\vec{E}_{o_i} \bullet \vec{E}_{o_2}\right)\underbrace{\left\{\cos\left[2\pi(\nu_1 + \nu_2)t + \varphi_1(t) + \varphi_2(t)\right]\right\}}_{\substack{A.C.\ current\\ in\ optical\ freq.}} + \end{aligned}$$

$$\left(\vec{E}_{o_i} \bullet \vec{E}_{o_2}\right)\underbrace{\left\{\cos\left[2\pi(\nu_1 - \nu_2)t + \varphi_1(t) - \varphi_2(t)\right]\right\}}_{\substack{\textit{A.C. current} \\ \textit{in} \text{ microwave} \textit{freq.}}}. \tag{4.7}$$

Because no detector responds as fast as optical frequencies and the *D.C.* components on the right hand side of Eq. (4.7) do not affect the overall frequency, only the last term above may be detectable, providing ν_1 and ν_2 are close to each other. Therefore, the effective current $i_H(t)$ generated by the two laser beams $\vec{E}_1$ and $\vec{E}_2$ are given by

$$i_H(t) = \left(\vec{E}_{o_1} \cdot \vec{E}_{o_2}\right) \cos\left[2\pi(\nu_1 - \nu_2)t + \varphi_1(t) - \varphi_2(t)\right], \tag{4.8}$$

where the effective frequency is the difference between the two laser frequencies ν_1 and ν_2, which is the so-called heterodyne beat frequency

$$\nu_H = \nu_1 - \nu_2. \tag{4.9}$$

As shown in Eq. (4.8), optimization of the heterodyne signal at the detector occurs when the two laser beams are collinear with electric fields in the same direction. As the photodetector current $i_H(t)$ flows through the resistive load R_d in the detector, a voltage across the load is generated

$$V_H(t) = i_H(t) R_d. \tag{4.10}$$

This heterodyne voltage $V_H(t)$ is amplified and input to a spectrum analyzer (*Hewlett-Packard Model 8566B*) , which determines the power spectral density $S_p(\nu)$ of the amplified heterodyne voltage

$$V_{H_M}(t) = M\, V_H(t) = \left(MR_d\right) i_H(t) \;\propto\; i_H(t), \tag{4.11}$$

where M is the amplification factor. According to the *Wiener-Khintchine* theorem[5] as mentioned in Section 2.1, the power spectrum $S_p(\nu)$ of $V_{H_M}(t)$ is given by the *Fourier* transform of the autocorrelation function of $V_{H_M}(t)$

$$S_p(\nu) = \mathcal{F}\left\{\left\langle V_{H_M}(t)V^*_{H_M}(t-\tau)\right\rangle\right\} \propto \mathcal{F}\left\{\left\langle i_H(t)i^*_H(t-\tau)\right\rangle\right\}, \tag{4.12}$$

where $\mathcal{F}\{\ \}$ indicates the *Fourier* transform of the bracketed expression and $< >$ denotes the time-averaged value of the autocorrelation function of the bracketed expression. The autocorrelation of $i_H(t)$ is given by

$$\begin{aligned} R(\tau) &= \left\langle i_H(t)i^*_H(t-\tau)\right\rangle \\ &= \frac{1}{4}\left|\vec{E}_{o1}\bullet\vec{E}_{o2}\right|^2\left\langle e^{i[\omega_H\tau+\Delta\varphi_1(\tau)-\Delta\varphi_2(\tau)]} + e^{-i[\omega_H\tau+\Delta\varphi_1(\tau)-\Delta\varphi_2(\tau)]}\right\rangle, \end{aligned} \tag{4.13}$$

where

$$\begin{aligned} \Delta\varphi_1(\tau) &\equiv \varphi_1(t)-\varphi_1(t-\tau), \\ \Delta\varphi_2(\tau) &\equiv \varphi_2(t)-\varphi_2(t-\tau), \end{aligned} \tag{4.14}$$

are the phase changes within the interval τ as defined by $\Delta\varphi$ in Eq. (2.15). The second term in the brackets in Eq. (4.13) is symmetrical to the first term in spectrum and will be neglected from now on. This simplifies Eq.(4.13) into the form of

$$R(\tau) = \frac{1}{4}\left|\vec{E}_{o1}\bullet\vec{E}_{o2}\right|^2 e^{i\omega_H\tau}\left\langle e^{i\Delta\varphi_1(\tau)}\, e^{-i\Delta\varphi_2(\tau)}\right\rangle. \tag{4.15}$$

Because the phases $\varphi_1(t)$ and $\varphi_2(t)$ are independent so that the autocorrelation for the two phases can be separated as follows

$$R(\tau) = \frac{1}{4}\left|\vec{E}_{o1} \bullet \vec{E}_{o2}\right|^2 e^{i\omega_H \tau} \left\langle e^{i\Delta\varphi_1(\tau)} \right\rangle \left\langle e^{-i\Delta\varphi_2(\tau)} \right\rangle. \tag{4.16}$$

Comparing Eq. (4.16) with Eq. (2.14), the result for $R(\tau)$ in Eq. (2.19) can be applied to Eq. (4.16)

$$\begin{aligned} R(\tau) &= \frac{1}{4}\left|\vec{E}_{o1} \bullet \vec{E}_{o2}\right|^2 e^{i\omega_H \tau} e^{-D_1|\tau|} e^{-D_2|\tau|} \\ &= \frac{1}{4}\left|\vec{E}_{o1} \bullet \vec{E}_{o2}\right|^2 e^{i\omega_H \tau} e^{-(D_1+D_2)|\tau|}, \end{aligned} \tag{4.17}$$

where D_1 and D_2 are the phase diffusion coefficients as defined in Eq. (2.17). Referring to Eqs. (2.20-2.21), *Fourier* transforming Eq.(4.17) yields the power spectrum $S_p(\nu)$ of the beat signal

$$S_p(\nu) = \frac{\left|\vec{E}_{o1} \bullet \vec{E}_{o2}\right|^2}{2(D_1 + D_2)} \frac{1}{1 + \left[\dfrac{(\nu - \nu_H)}{(D_1 + D_2)/2\pi}\right]}. \tag{4.18}$$

Therefore, in the case of randomly fluctuating phases $\varphi_1(t)$ and $\varphi_2(t)$, the heterodyne signal retains the features of the two sources. Eq. (4.18) indicates that the lineshape $S_p(\nu)$ of the heterodyne signal is still *Lorentzian* but centered at the beat frequency ν_H. The linewidth $\Delta\nu_H$ of the heterodyne signal is equal to the sum of the two laser linewidths $\Delta\nu_1$ and $\Delta\nu_2$

$$\begin{aligned} \Delta\nu_H &= \frac{(D_1 + D_2)}{\pi} = \frac{D_1}{\pi} + \frac{D_2}{\pi} \\ &= \Delta\nu_1 + \Delta\nu_2, \end{aligned} \tag{4.19}$$

where $\Delta\nu_1$ and $\Delta\nu_2$ are given by Eqs. (2.21-2.23).

A schematic of the heterodyne setup is shown in Fig. 4.6. Recall that the design of the grating-tuned external-cavity diode laser provided two opposite beams as shown in Fig. 4.1. The weaker beam from each laser was focused into a power meter separately. The two stronger beams from two lasers were combined on a beam splitter. In order to maximize the heterodyne signal at the detector, a confocal scanning *Fabry-Perot* interferometer and a series of apertures were employed to insure beam collinearity. A linear polarizer was inserted for maximum dot product of the two electrical fields $\vec{E}_{o_1}$ and $\vec{E}_{o_2}$ as suggested by Eq. (4.8). The transmission axis of the polarizer was made to coincide with the bisector of the angle formed by the two electric fields. Coarse frequency line coincidence was achieved by monitoring the laser output through a spectrometer with a resolution of *1 A°*. Line overlap was accomplished with a combination of grating tilting and current as well as temperature tunings. The single-mode operation was verified by the scanning *Fabry-Perot* interferometer. In all experiments, beam isolators were used to prevent optical feedback from the spectrometer and the *Fabry-Perot* interferometer. Feedback from the *Ge* avalanche photodetector (*Newport Corp., Model 877*) was avoided by defocusing the beam and all lenses were tilted slightly off axis.

The powers of the two lasers were approximately fixed at *5 mW*. The *Lorentzian* power spectra S_p of the heterodyne signals between the two lasers operating from *935 nm* to *945 nm* were recorded by a *LabView* program. The linewidth of the heterodyne spectrum at each wavelength was evaluated by the least-squares fit to the measured lineshape. A quick way to determine the - *3 dB* (*FWHM*) linewidth in log scale is to measure the averaged full width at *40 dB* down from the peak intensity. It is easy to prove that the - *3 dB* linewidth is equal to the - *40 dB* width divided by *100*. The uncertainty associated with the value for the *3 dB* linewidth is thus the uncertainty (the

width of noise) at this - *40 dB* level divided by *100*. Consequently, the plot of linewidth of the heterodyne beat signal between the two lasers as a function of wavelength was obtained.

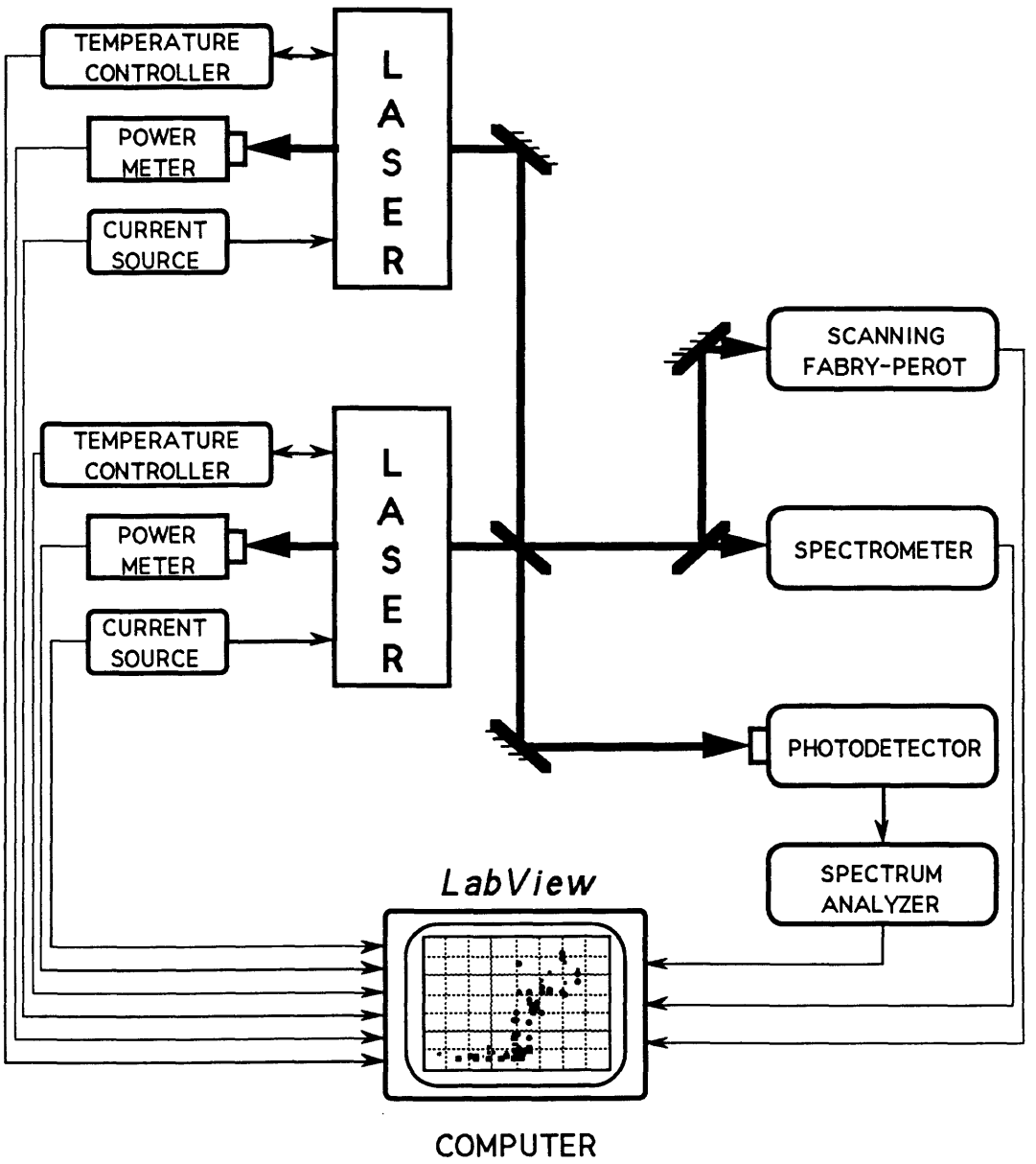

Fig. 4.6 Block diagram of the heterodyne setup.

CHAPTER 5

RESULTS AND DISCUSSION

A series of experiments have been conducted with two free-running grating-tuned *CW* single-mode external-cavity strained quantum-well *InGaAs/AlGaAs GRINSCH* diode lasers. Measurements include the power spectrum at constant current, threshold current spectrum, heterodyne linewidth-inverse power characteristics, heterodyne linewidth spectrum at constant power, and frequency stability test. These experimental data are compared with the calculation using the simple interband mode as described in Chapter 3. Features of the wavelength dependence of the spectral linewidth and the amplitude-phase coupling factor α are therefore extracted from these comparisons.

Wavelength tunability is one of the prerequisite properties of the laser for the study on the wavelength dependence of the laser linewidth. The tunability of one of the two grating-tuned *CW* single-mode external-cavity diode laser used in this experiment is illustrated in Fig. 5.1, in which the laser output power is measured and plotted as a function of wavelength at a constant current $I = 80\ mA$. This power spectrum shows a tuning range from *925 nm* to *955 nm*, providing a laser power $P_o \geq 5\ mW$. In addition, a power spectrum also reveals the gain profile of the diode laser; Fig. 5.1 implies that the maximum gain occurs at wavelengths around *945 nm*.

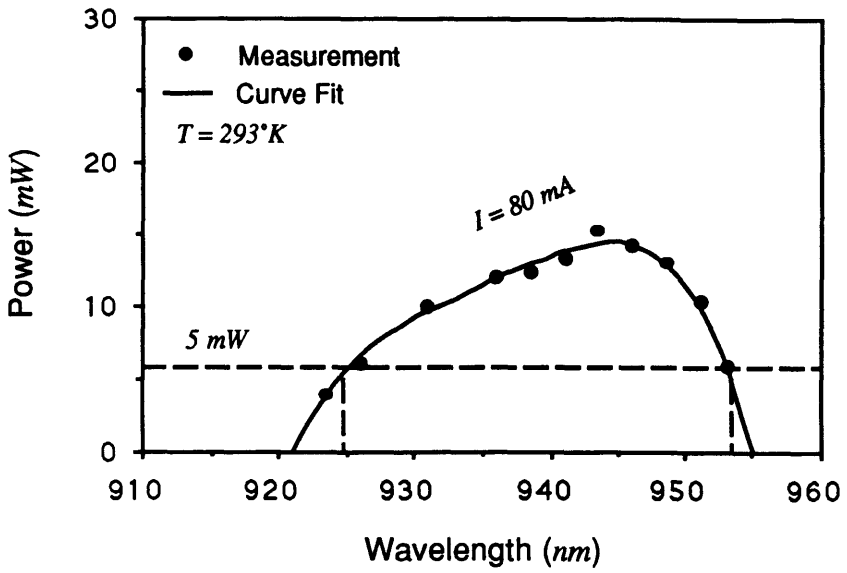

Fig. 5.1 Plot of laser output power as a function of wavelength for laser diode #1.

Because the threshold current for a laser decreases with increasing gain of the laser medium, the minimum threshold current of this diode laser is expected to occur at *945 nm* where the power and, hence, the gain is peaked. This expectation is justified with a measurement of the threshold current as a function of wavelength. As shown in Fig. 5.2, the valley of the measured spectrum of threshold current takes place near *945 nm* as expected. In addition, the calculated threshold current based on the simple interband model, using $x = 0.16$, shows a good agreement in comparison with the measured one. This agreement supports the use of the simple interband model for the calculation of the amplitude-phase coupling factor α.

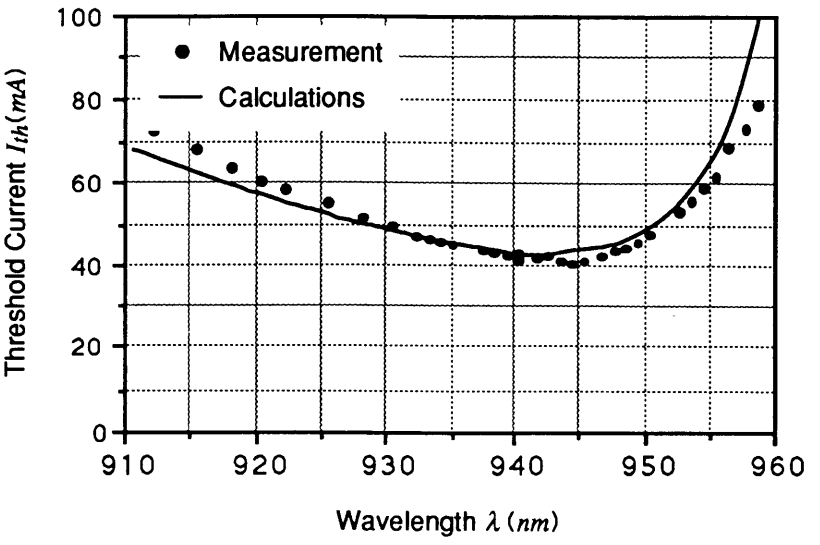

Fig. 5.2 Comparison between the measured (dots) and the calculated (solid curves) threshold current I_{th} as a function of wavelength λ, using $x = 0.16$ for laser #1.

The comparison for α between calculation and measurement is performed in terms of laser linewidth $\Delta\nu$, because α can be deduced from $\Delta\nu$ through a relation as given by Eq. (2.50)

$$\Delta\nu(\lambda) = \Delta\nu_{S-T}\left[1+\alpha^2(\lambda)\right], \tag{5.1}$$

where the *Schawlow-Townes* linewidth $\Delta\nu_{S-T}$ can be calculated according to Eq. (2.36). Therefore, measuring the linewidth spectrum of the heterodyne beat signal between two lasers provides the wavelength dependence of linewidth and of α simultaneously. Heterodyne beat signal between the two free-running external-cavity strained quantum-well $In_{0.14}Ga_{0.86}As$ / $Al_{0.2}Ga_{0.8}As$ *GRINSCH* diode lasers used in this experiment is as shown in Figs. 5.3 (a) through (d) for $\lambda = 940$ *nm*, in which the vertical scale is *10 dB/Div*. The center (beat) frequency, span (horizontal scale), scan time, and resolution bandwidth of each measurement (plot) are given in the right upper corner. Fig. 5.3 (a)

shows that the heterodyne measurement was taken when the two lasers *#1* and *#2* were observed in stable single-mode operation on the scanning *Fabry-Perot* interferometer as shown in the inset. The center frequency of *678 MHz* of this beat signal is then the difference between the two laser frequencies. The most significance out of this heterodyne beat spectrum is its *Lorentzian* lineshape which identifies itself arising from the random phase noise. Applying least-squares *Lorentzian* fit (thick black solid curve) to the bush-like data, one obtains a *20-kHz* linewidth (*FWHM*) of the spectrum at *940 nm* wavelength at a fixed 5 *mW* output power from each laser. The uncertainty associated with the *FWHM* linewidth is easily determined: the noise width at *40 dB* down from signal peak divided by *100*, as discussed in Section 4.3. In this particular case, the uncertainty at - *60 dB* (= - *20 dB* - *40 dB*) is ~ *600 kHz* on one wing, consequently, the uncertainty for the linewidth is ~ *6 kHz*. The values for the linewidth, its uncertainty, and the output power are given on the left upper corner of each plot.

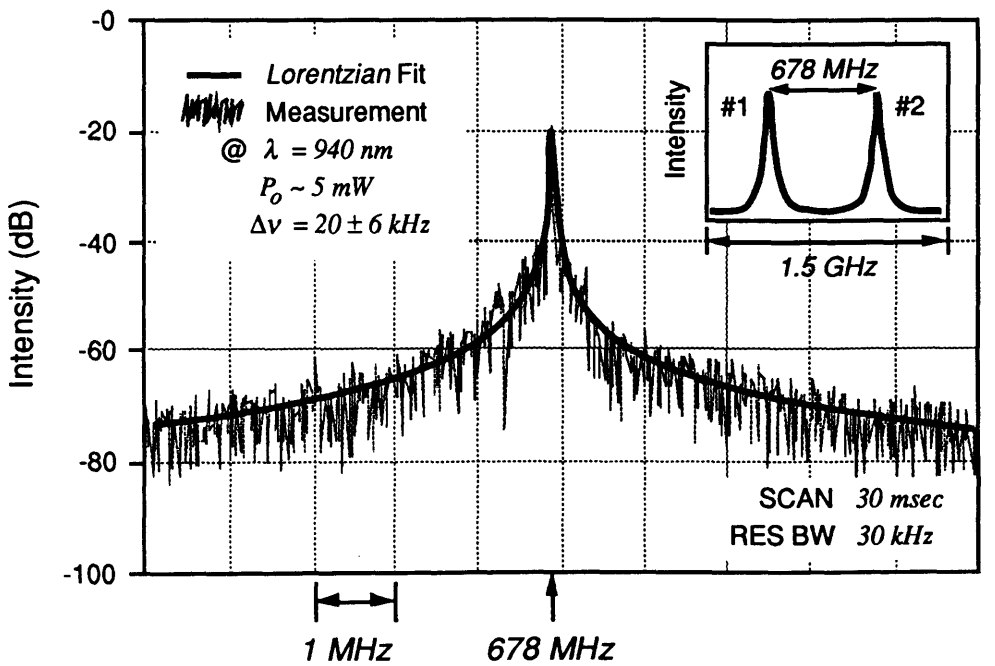

(a) $P_O = 5\ mW$

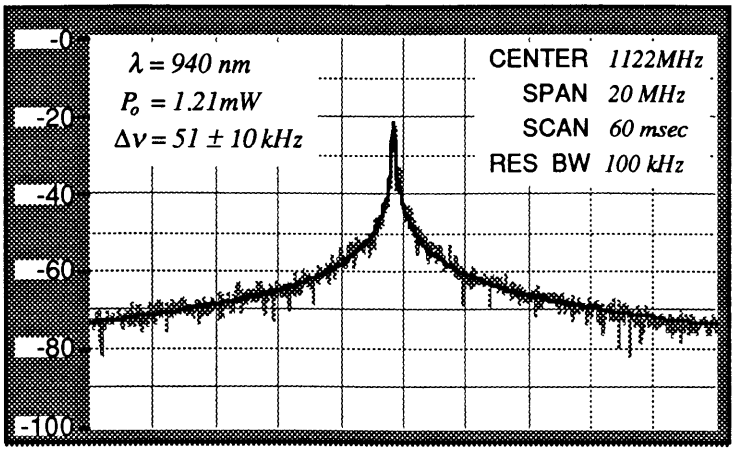

(b) $P_o = 1.21\ mW$

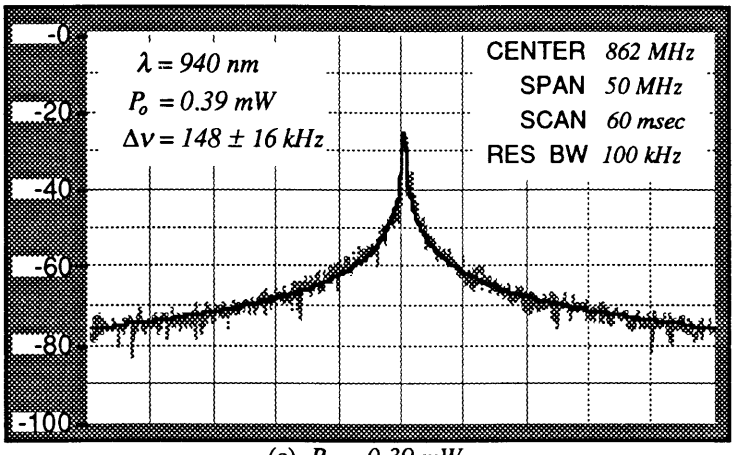

(c) $P_o = 0.39\ mW$

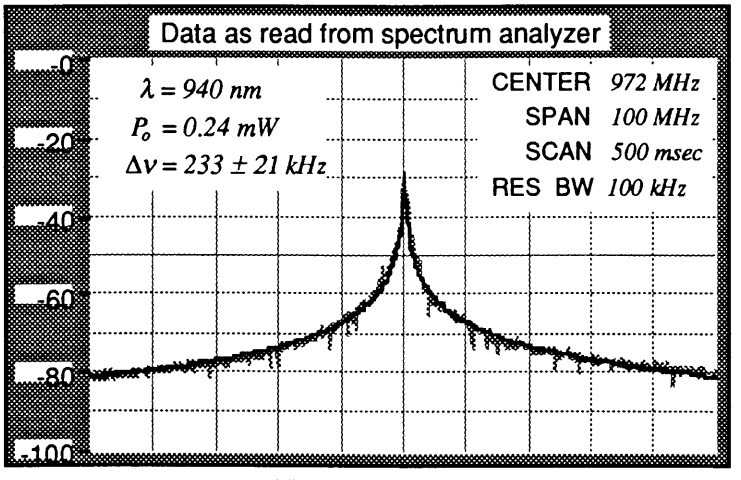

(d) $P_o = 0.24\ mW$

Fig. 5.3 Heterodyne beat signal between two free-running external-cavity diode lasers: *#1* and *#2* at *940 nm* for different output powers. The thick black solid curves are *Lorentzian* fits to the data.

Because *Lorentzian* function decreases less rapidly than *Gaussian* function for frequencies away from the center frequency, the lineshape at *40 dB* down from the beat signal peak is more *Lorentzian* than that at *3 dB* down in the presence of the extrinsic noise; the lineshape is then, more or less, a mixture of *Lorentzian* with *Gaussian* functions. Therefore, the *40 dB* width retains more accurate value for the linewidth of the *Lorentzian* component of the heterodyne beat signal than the *3 dB* width does; this method does not require a spectrum analyzer with a very high resolution bandwidth. In order to determine the relative contribution to the spectral linewidth from the extrinsic noise, a long heterodyne measurement was carried. As shown in Fig. 5.4, the frequency jitter between the two free-running lasers displays a *Gaussian* envelop with a linewidth of approximately *90 kHz* in a *60 sec* scan: a jitter rate of *1.5 kHz/sec*. This jitter rate implies that the frequency jitter in a short *100 msec* scan is *150 Hz*, which is relatively less than the observed linewidth on the order of tens of *kHz*. Therefore, this helps the justification for the early assumption that the extrinsic noise is negligible in this work.

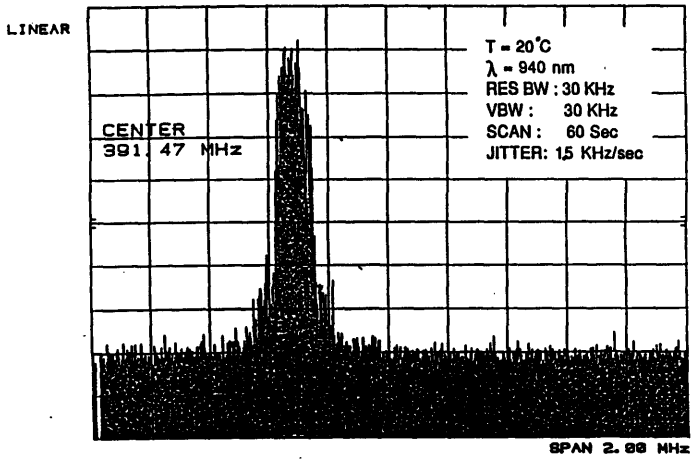

Fig. 5.4 Frequency jitter between two free-running *InGaAs* external-cavity diode lasers.

Because the *Schawlow-Townes* linewidth $\Delta\nu_{S\text{-}T}$ is inversely proportional to the output power, one can repeat the same procedure with different output power P_o at *940 nm* and plot the linewidth of the heterodyne beat signal as a function of inverse power as shown in Fig. 5.5. It is found that the extrapolation of the heterodyne linewidth-inverse power curve into the linewidth axis shows a finite linewidth $\Delta\nu_{PI} \sim 7.5\ kHz$ at infinite power. Other than this power-independent component $\Delta\nu_{PI}$, the power-dependent component does display the linearity with respect to the reciprocal power, which agrees with our analytical expression for the overall linewidth including the shot noise contribution as discussed in Section 2.3.

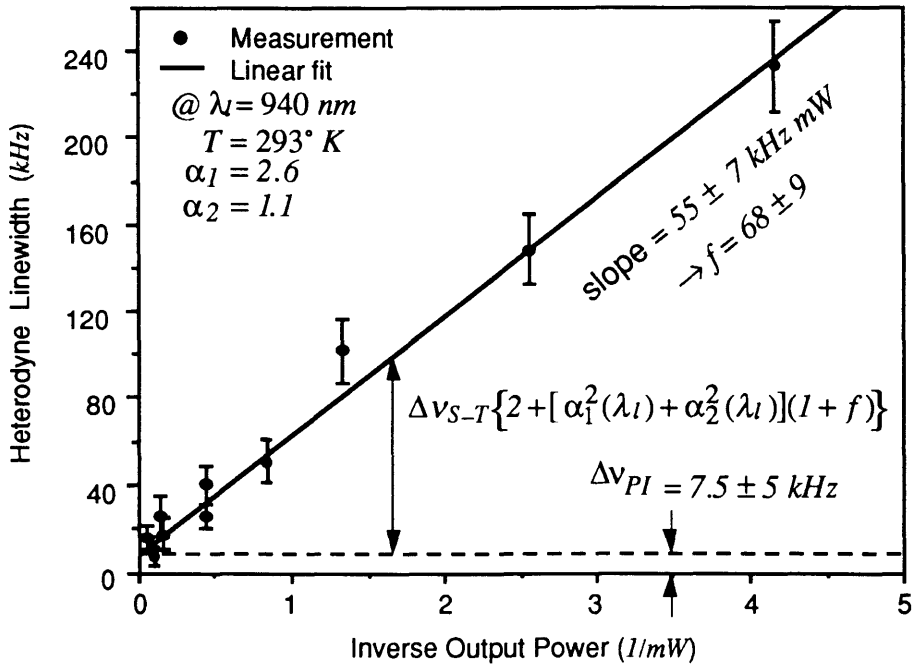

Fig. 5.5 Measured linewidth of the heterodyne beat signal as a function of inverse output power.

Repeating the same procedure for heterodyne linewidth measurement over the tuning range yields the plot of heterodyne linewidth as a function of wavelength as shown in Fig. 5.6. Data shows that the heterodyne linewidth displays a sharp rise for wavelength above *940 nm* but remains relatively constant at approximately *10 kHz* below *940 nm*. Recall that, as discussed in Section 4.3, the linewidth of the heterodyne signal $\Delta\nu(\lambda_l)$ is the sum of the two laser linewidths $\Delta\nu_1(\lambda_l)$ and $\Delta\nu_2(\lambda_l)$; *Lorentzian* linewidth is additive. Considering the shot noise model, which includes f and $\Delta\nu_{PI}$ due to shot noise, the linewidth of the heterodyne beat signal is given in the general form

$$\begin{aligned}\Delta\nu(\lambda_l) &= \Delta\nu_1(\lambda_l)+\Delta\nu_2(\lambda_l)\\ &= \Delta\nu_{S-T}\left[1+\alpha_1^2(\lambda_l)(1+f)\right]+\Delta\nu_{PI_1}+\Delta\nu_{S-T}\left[1+\alpha_2^2(\lambda_l)(1+f)\right]+\Delta\nu_{PI_2}\\ &= \Delta\nu_{S-T}\left\{2+\left[\alpha_1^2(\lambda_l)+\alpha_2^2(\lambda_l)\right](1+f)\right\}+\left(\Delta\nu_{PI_1}+\Delta\nu_{PI_2}\right)\\ &= \Delta\nu_{S-T}\left\{2+\left[\alpha_1^2(\lambda_l)+\alpha_2^2(\lambda_l)\right](1+f)\right\}+\Delta\nu_{PI}, \qquad (5.2)\end{aligned}$$

with

$$\Delta\nu_{S-T} = 20Hz \qquad (5.3)$$

$$\Delta\nu_{PI} = \Delta\nu_{PI_1}+\Delta\nu_{PI_2}, \qquad (5.4)$$

where $\Delta\nu_{S\text{-}T}$ is calculated as given by Eq. (3.23), and $\Delta\nu_{PI}$ is the total power-independent linewidth of the two lasers and is 7.5 ± 5 *kHz* at *940 nm* as shown in Fig. 5.5. In comparing the measured linewidth with the two calculated linewidths due to spontaneous emission as shown in Fig. 3.7, the sum of the two calculated linewidths, with $x = 0.14$ (dominant) and $x = 0.16$, respectively, appears to fit data in shape except in different scales. The agreement on shape, especially on the turning point at $\lambda = 940$ *nm*, indicates

that the second diode laser has an alloy composition $x = 0.14$; this second diode was broken before we could carry out the measurement for threshold current spectrum which suggests $x = 0.16$ for the first diode. At this particular wavelength $\lambda = 940\ nm$, using the calculated values for $\alpha_1(940nm) = 2.6$ for $x = 0.14$ and $\alpha_2(940nm) = 1.1$ for $x = 0.16$ and the observed value for $\Delta\nu_{PI} = 7.5 \pm 5kHz$ it can be shown that $f \cong 68 \pm 9$. Assuming f and $\Delta\nu_{PI}$ are weakly wavelength dependent, combining $f = 77$ (maximum value for f) and $\Delta\nu_{PI} = 6\ kHz$ with the calculated values for α_1 and α_2 as a function of wavelength, calculation for the linewidth of the heterodyne beat signal versus wavelength according to Eq. (5.3) is found in qualitative agreement with the measurement as shown in Fig. (5.5). It should be pointed out that this number 68 ± 9 for f depends upon the calculated values for α; both are complementary to each other. These values for $\Delta\nu_{PI}$ and for f deduced from α and heterodyne linwidth are compared with their calculated values using the shot noise model as follows:

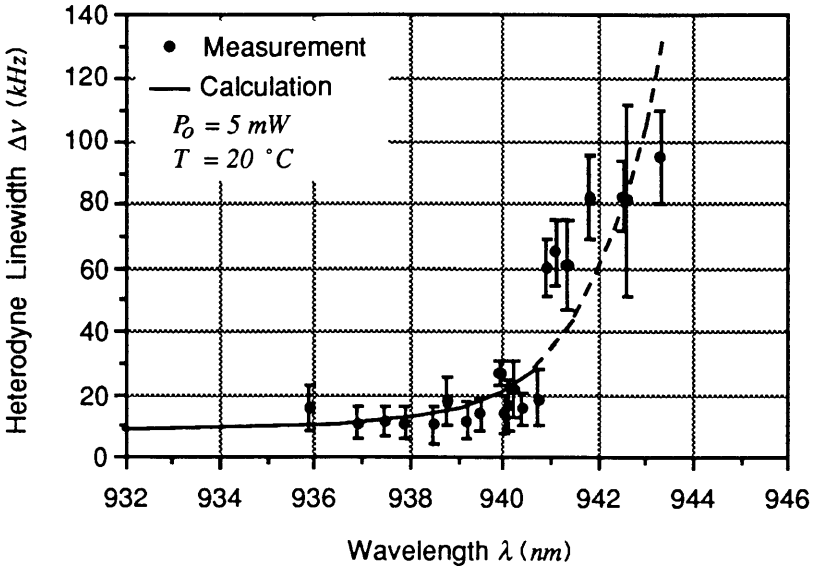

Fig. 5.6 Measured (dots) and calculated [solid curve: $\Delta\nu_1(x=0.14) + \Delta\nu_2(x=0.16)$ with $f = 77$ and $\Delta\nu_{PI} = 6\ kHz$] linewidth (*FWHM*) of the heterodyne beat signal as a function of wavelength.

To calculate the factor f, consider the parameters involved in the definition for f as given by Eq. (2.53):

$$f \equiv \frac{\Delta\eta_{stat}}{\Delta\eta_{sp}}. \tag{5.5}$$

Here f represents the ratio of the statistical fluctuations (shot noise) in the carrier population $\Delta\eta_{stat}$ to the fluctuations in the carrier population $\Delta\eta_{sp}$ caused by amplitude fluctuation due to spontaneous emission. Comparison between the calculated value for f and the deduced value 68 ± 9 for f is necessary for the justification of this shot noise model.

The calculation for f involves the following values: $R_{HR} \cong 1$, $R_m \cong 25\%$, $L_a = 1\ mm$, $n'_{la} = 3.6$, $\gamma_a = 3.5\ cm^{-1}$, $L_p = 10\ cm$, $V = 2 \times 10^{-10} cm^3$, and $\Gamma_s = 0.15$, $N_{th} \sim 1.5 \times 10^{18} cm^{-3}$, and $\tau_{sp} \sim 1.3 \times 10^{-13}\ sec$. The values for the last three parameters: optical confinement factor Γ_s, threshold carrier density N_{th}, and the spontaneous emission lifetime τ_{sp} are calculated from our simple interband model. The remaining values are taken from Table 3.3. Note that both fluctuations in carrier population $\Delta\eta_{stat}$ and $\Delta\eta_{sp}$ count the total number of carriers instead of the carrier density. Hence, the dimensionless η_{th}, the total number of threshold carrier population, is the product of the threshold carrier density N_{th} and the volume V of the active layer as given by

$$\eta_{th} = V \times N_{th} = 3 \times 10^8. \tag{5.6}$$

Subsequently, the statistical fluctuations in the carrier population $\Delta\eta_{st}$ are then obtained:

$$\Delta\eta_{th} = \sqrt{\eta_{th}} = 1.73 \times 10^4. \tag{5.7}$$

Substituting the appropriate values into the following expression for $\Delta\eta_{sp}$ yields

$$\Delta\eta_{sp} = \frac{\tau_{sp}R_{sp}}{\Gamma_s} = \frac{\tau_{sp}}{\Gamma_s}\left(\frac{c}{n'_{la}L_a + L_p}\right)\left[\gamma_a La + \frac{1}{2}\ln\left(\frac{1}{R_{HR}R_m}\right)\right] \sim 26. \tag{5.8}$$

Consequently, f is given by

$$f = \frac{\Gamma_s\Delta\eta_{stat}}{\Delta\eta_{sp}} = \frac{1.73\times10^4}{26} \approx 660 >> 1. \tag{5.9}$$

Thus the calculated f and the observed value of f differ by a factor of *10*. As shown in Eq. (5.2), f and α are complementary to each other. The lower observed value of f may also imply that *90%* of the shot noise is suppressed.

Applying this shot noise model to the solitary diode laser in *Fleming* and *Mooradian's*[3] work, using the values: $R_m = R_{HR} \cong 0.32$, $n'_{la} = 3.6$, $L_a = 300\ \mu m$, $\gamma_a = 45\ cm^{-1}$, $L_p = 0$, $\Gamma_s = 0.4$, $V = 4\times10^{-11}cm^3$, $\tau_{sp} \sim 2\times10^{-13}\ sec$, and $\eta_{th} = V\times N_{th} = 1.8\times10^8$, one obtains

$$\Delta\eta_{stat} \sim 1.35\times10^4, \tag{5.10}$$

and

$$\Delta\eta_{sp} \sim 3.75\times10^3, \tag{5.11}$$

which yields

$$f = \frac{\Delta\eta_{stat}}{\Delta\eta_{sp}} = \frac{13500}{3750} \approx 3.6. \tag{5.12}$$

Notice that their calculated $f = 3.6$ is relatively negligible in comparison with our calculated $f = 660$. This is the reason why there is relatively little difficulty in

interpreting their value of the linewidth by only considering the spontaneous emission effect including α^2; this small f could have been easily absorbed into α^2 unintentionally. On the other hand, comparing Eqs. (5.8) and (5.11) for $\Delta\eta_{sp}$ and Eqs. (5.6) and (5.10) for $\Delta\eta_{stat}$, considerable linewidth reduction using external-cavity suppresses the fluctuations in the carrier population $\Delta\eta_{sp}$, from *3750* to *26*, due to spontaneous emission, yet, the statistical fluctuation $\Delta\eta_{stat}$ remains unaffected. Therefore, as shot noise becomes dominant, it results in a large f. The competition between the spontaneous emission and the shot noise, which is responsible for f, is the new physics to the additional linewidth broadening.

Shot noise affects the linewidth not only through the *AM-FM* coupling in the active medium but also through the shift in cavity-mode frequency. Modifying *Welford* and *Mooradian*'s[3] phenomenological model for the power-independent linewidth $\Delta\nu_{PI}$ for each laser, simply replacing the phase refractive index n'_{la} with the group refractive index $n'_{la}|_g$, as given by

$$\left|\Delta\nu_{PI_i}\right| = \Gamma_s \nu_l \left(\frac{L_a}{n'_{la}L_a + n'_{lp}L_p}\right)\left[\frac{d\left(n'_{la}|_g\right)}{d(\eta_{th})}\right]\Delta\eta_{st}, \tag{5.13}$$

with

$$n'_{la}|_g = n'_{la} + \frac{\upsilon_l}{n'_{la}}\left(\frac{dn'_{la}}{d\upsilon_l}\right) = n'_{la} - \frac{\lambda_l}{n'_{la}}\left(\frac{dn'_{la}}{d\lambda_l}\right), \tag{5.14}$$

where η_{th} is the total carrier population as given by Eq. (5.7). Because $n'_{la}|_g$ may be very different from n'_{la} near resonance depending on both the magnitude and sign of the dispersive factor $\left(\frac{dn'_{la}}{d\lambda_l}\right)$ as shown in Fig. 3.6 (a), the factor $\left[\frac{d\left(n'_{la}|_g\right)}{d(\eta_{th})}\right]$ in Eq. (5.13) is

very much wavelength dependent other than temperature dependent. For simplicity in a qualitative picture for $\Delta\nu_{PI}$, taking the average of the measured value at room temperature for $\left[\frac{d\left(n'_{la}\big|_g\right)}{d(\eta_{th})}\right]$ ($\sim -5 \times 10^{-12}$) from *Welford* and *Mooradian*'s[3] work, and substituting our appropriate values into the remaining parameters as shown in Eq. (5.13) for $\Delta\nu_{PI_i}$, one obtains

$$2\times\left|\Delta\nu_{PI_i}\right| = 2\times\left[0.15\times\left(3.2\times10^{14}\right)\left(\frac{0.1}{3.6\times0.1+1\times10}\right)\left(5\times10^{-12}\right)\sqrt{3\times10^{8}}\right]$$

$$\approx 80\ kHz. \qquad (5.15)$$

The additional factor of *2* accounts for the sum of $\Delta\nu_{PI_1}$ and $\Delta\nu_{PI_2}$ for the two lasers, respectively. In comparison with our observed value for $\Delta\nu_{PI} \sim 7.5 \pm 5\ kHz$, a factor of *10* lower in magnitude in our strained quantum-well laser diode may account for the strain effect which reduces the differential refractive index per carrier per unit volume $\left(\frac{dn'_{la}}{dN}\right)$. However, the consistency in the comparison of f and $\Delta\nu_{PI}$ for both components of linewidth may imply that the shot noise is partially suppressed.

The idea of statistical fluctuations in population seems against the laser dynamics in lasing condition in which the population inversion (carrier) density is supposed to be clamped at its threshold value and $\Delta\eta_{stat} = 0$. However, this argument may be true for a completely homogeneous medium, and is not necessarily the case for an inhomogeneous medium. From this point of view, the simple form for $\Delta\eta_{stat}$ as given above represents the limiting case of a completely inhomogeneous medium. Therefore, the shot noise-induced linewidth may be well below the calculated value using the simple relation.

This shot noise model provides a qualitative interpretation for the discrepancy between the observed linewidth and the calculated linewidth due to spontaneous emission only. The competition between the shot noise and spontaneous emission determines the magnitude of f and the shot noise is responsible for the power-independent linewidth. This model shows its consistency for external-cavity diode lasers in this work and for solitary diode lasers in previous work.

CHAPTER 6

CONCLUSIONS

The semiconductor diode laser has proven to be an ideal medium for the study of fundamental noise processes in lasers. The wavelength dependence of the spectral linewidth of a grating-tuned *CW* single-mode external-cavity strained quantum well *InGaAs/AlGaAs GRINSCH* diode laser has been investigated for operation at room temperature (*20 °C*). Measurements include the power spectrum at a constant injection current, threshold current spectrum, linewidth-inverse power characteristics at a fixed wavelength, and linewidth spectrum at a constant power. Theoretical work is the calculation for the amplitude-phase coupling factor α as a function of wavelength using a simple interband model. Based on the experimental results, we have proposed shot noise in the carrier population as an additional source for the spectral linewidth.

The overall intrinsic laser linewidth consists of a power-dependent component and a power-independent component. The well-known *Shawlow-Townes* linewidth $\Delta\nu_{S\text{-}T}$ considers only the spontaneous emission and falls into the category of power-dependent linewidth. This power-dependent linewidth involves α^2, which is wavelength-dependent. Our calculation for α indicates a sharp rise in the power-dependent linewidth spectrum as the laser photon energy approaches the energy band gap of the semiconductor. This feature in shape is observed in the linewidth spectrum using the heterodyne technique. However, there is a big discrepancy in magnitude between the observed linewidth and calculated linewidths due to spontaneous emission alone.

The shot noise provides a qualitative interpretation for the discrepancy between the observed power-dependent linewidth and the calculated linewidth due to spontaneous

emission only. For power-dependent linewidth, although shot noise and spontaneous emission are two independently intrinsic noise sources, they affect the laser frequency through the same final channel, that is, the fluctuations in phase. This is the reason why the *Shawlow-Townes* linewidth $\Delta\nu_{S\text{-}T}$ is a common factor in every component of the power-dependent linewidth due to different noises. Shot noise is also responsible for the power-independent component of linewidth $\Delta\nu_{PI}$.

Because shot noise also depends on wavelength through its dependence on the threshold carrier density, f and $\Delta\nu_{PI}$ should depend on wavelength too. However, linewidth-inverse power measurement was conducted at one wavelength in this work only. Hence, only values for f and $\Delta\nu_{PI}$ were deduced at this wavelength. For further study of the shot noise contribution, the wavelength dependence of f and $\Delta\nu_{PI}$ must be measured.

REFERENCES

1. A. L. Schawlow and C. H. Townes, "Infrared and Optical Masers," *Phys. Rev.*, Vol. 112, pp. 1940-1949, 1958.

2. M. Lax, "Quantum Noise V: Phase Noise in a Homogeneously Broadened Maser," in *Physics and Quantum Electronics*, P. L. Kelly, B, Lax, and P. E. Tannenwald, Eds., New York: Mcgraw-Hill, 1966, pp. 735-747.

3. C. H. Henry, "Theory of the Linewidth of Semiconductor Lasers," *IEEE J. Quantum Electron.*, Vol. QE-18, pp. 259-264, 1982.

4. D. Welford and A. Mooradian, "Observation of linewidth broadening in (GaAl)As diode lasers due to electron number fluctuations," *Appl. Phys. Lett.*, Vol. 40, pp. 560-562, 1982.

5. See, for example, H. E. Rowe, *Signals and Noise in Communication Systems*, New York: D. Van Nostrand, 1965, pp. 37.

6. M. Lax, "Classical noise V: Noise in self-sustained oscillators," *Phys. Rev.*, Vol. 160, pp. 290-307, 1967.

7. A. Yariv, *Quantum Electronics*, New York: John Wiley, 1989, p. 165.

8. C. H. Henry, R. A. Logan, and F. R. Merritt, "Measurement of gain and absorption spectra in AlGaAs buried heterostructure lasers," *J. Appl. Phys.* Vol. 51, pp. 3042-3050, 1980.

9. E. Yablonovitch and E. O. Kane, Correction to "Reduction of Lasing Threshold Current Density by the Lowering of Valence Band Effective Mass,: *IEEE J. Lightwave Tech.*, Vol. LT-4, p. 961, 1986.

10. E. Yablonovitch and E. O. Kane, "Reduction of Lasing Threshold Current Density by the Lowering of Valence Band Effective Mass," *IEEE J. Lightwave Tech.*, Vol. LT-5, pp. 504-506, 1986.

11. D. Welford and A. Mooradian, "Output power and temperature dependence of the linewidth of single-frequency cw (GaAl)As diode lasers," *Appl. Phys. Lett.*, Vol. 40, pp. 865-867, 1982.

12. J. Harrison, *SPECTRAL CHARACTERISTICS OF SEMICONDUCTOR DIODE LASERS*, Ph.D. Thesis, Massachusetts Institute of Technology, Department of Electrical Engineering and Computer Science, Cambridge, MA, 1987, p. 15.

13. M. W. Fleming and A. Mooradian, "Spectral characteristics of external-cavity controlled semiconductor lasers," *IEEE J. Quantum Electron.*, Vol. QE-17, pp. 44-59, 1981.

14. M. W. Fleming and A. Mooradian, "Fundamental line broadening of single-mode (GaAl)As diode lasers," *Appl. Phys. Lett.*, Vol. 38, pp. 511-513, 1981.

15. G. Lasher and F. Stern, "Spontaneous and stimulated recombination radiation in semiconductors," *Phys. Rev.*, Vol. 133A, pp. A553-563, 1964.

16. F. Stern, "Calculated spectral dependence of gain in excited GaAs," *J. Appl. Phys.*, Vol. 47, pp. 5382-5386, 1976.

17. H. K. Choi and C. A. Wang, "InGaAs/AlGaAs strained single quantum well diode lasers with extremely low threshold current density and high efficiency," *Appl. Phys. Lett.*, Vol. 57, pp. 321-323, 1990.

18. C. A. Wang and H. K. Choi, "Organometallic Vapor Phase Epitaxy of High-Performance Strained-Layer InGaAs-AlGaAs Diode Lasers,", *IEEE J. Quantum Electron.*, Vol. 27, pp. 681-686, 1991.

19. A. R. Adams, "Band-structure engineering for low-threshold high-efficiency semiconductor lasers,"", *Electron. Lett.*, Vol. 22, pp. 249-250, 1986.

20. J. M. Luttinger and W. Kohn, "Motion of electrons and holes in perturbed periodic fields," *Phys. Rev.*, Vol. 97, pp. 869-877, 1955.

21. H. C. Casey, Jr., and M. B. Panish, *Heterostructure lasers; Part A: Fundamental Principles*, Orlando, Florida: Academic Press, 1978.

22. G. H. Olsen, C. J. Nuese, and R. T. Smith, "The effect of elastic strain on energy band gap and lattice parameter in III-V compounds[a]," *J. Appl. Phys.*, Vol. 49, pp. 5523-5529, 1978.

23. C. P. Kuo, S. K. Vong, R. M. Cohen, and G. B. Stringfellow, "Effect of mismatch strain on band gap in III-V semiconductors," *J. Appl. Phys.*, Vol. 57, pp. 5428-5432, 1985.

24. G. Ji, D. Huang, U. K. Reddy, T. S. Henderson, R. Houdre, H. Morkoc, "Optical investigation of highly strained InGaAs-GaAs multiple quantum wells," *J. Appl. Phys.*, Vol. 62, pp. 3366-3373, 1987.

25. J. P. Loehr and J. Singh, "Theoretical Studies of the Effect of Strain on the Performance of Strained Quantum Well Lasers Based on GaAs and InP Technology," *IEEE J. Quantum Electron.*, Vol. 27, pp. 708-716, 1988.

26. R. M. Kolbas, N. G. Anderson, W. D. Laidig, Y. Sin, Y. C. Lo, K. Y. Hsieh, and Y. J. Yang, "Strained-Layer InGaAs-GaAs-AlGaAs Photopumped and Current Injection Lasers," *IEEE J. Quantum Electron.*, Vol. 24, pp. 1605-1613, 1988.

27. D. P. Pour, D. B. Gilbert, L. Elbaum, and M. G. Harvey, "Continuous, high-power operation of a strained InGaAs/AlGaAs quantum well laser," *Appl. Phys. Lett.*, Vol. 53, pp. 2371-2373, 1988.

28. E. D. Jones, S. K. Lyo, J. F. Klem, J. E. Schirber, M. C. Smith, and C. P. Tigges, "Simultaneous measurement of the conduction and valence-band masses in strained-layer structures," *Inst. Phys. Conf. Ser.* 96, pp. 243-247, 1988.

29. S. K. Lyo, E. D. Jones, "Valence-band energy dispersion in modulation-doped quantum wells: effect of strain and confinement on heavy- and light- hole mixing," *Inst. Phys. Conf. Ser.* 120, p. 588, 1991.

30. S. W. Corzine, R. H. Yan, and L. A. Coldren, "Simultaneous gain and phase shift and enhancement in periodic gain structure," *Appl. Phys. Lett.*, Vol. 67, pp. 4387-4389, 1990.

31. Peter S. Zory, Jr., *Quantum Well Lasers,* New York: Academic Press, 1993, p. 64.

32. H. Morkoc, B. Sverdlov, and G. Gao, "Strained Layer Heterostructures, and their Applications to MODFET's, HBT's, and Lasers," *Proceedings of the IEEE*, Vol. 81, pp. 493-556, 1993.

33. Peter S. Zory, Jr., *Quantum Well Lasers,* New York: Academic Press, 1993, p. 79.

34. S. Adachi, "GaAs, AlAs, and $Al_xGa_{1-x}As$: Material parameters for use in research and device applications," *J. Appl. Phys.*, Vol. 58, pp. R1-R29, 1985.

35. S. R. Chinn, P. S. Zory, and A. R. Reisinger, "A Model for GRINSCH SQW Diode Lasers," *IEEE J. Quantum Electron.*, Vol. QE-24, pp. 2191-2214, 1988.

36. S. R. Chinn, "Modal analysis of GRINSCH and triangular-well waveguides," *Applied Optics*, Vol. 23, pp. 3508-3509, 1984.

37. H. Kressel, and J. K. Butler, *Semiconductor Lasers and Heterojunction LED's*, New York: Academic Press, 1977.

38. G. P. Agrawal and N. K. Dutta, *LONG-WAVELENGTH SEMICONDUCTOR LASERS,* New York: Van Nostrand Reinhold, 1986, Chapters 3 and 9.

39. A. Yariv, *Quantum Electronics*, New York: John Wiley, 1989, p. 159.

3636-8